Advanced plasma flow simulations of cathodic-arc and ferroelectric plasma sources for neutralized drift compression experiments

Adam B. Sefkow, Ronald C. Davidson, and Erik P. Gilson

Plasma Physics Laboratory, Princeton University, Princeton, New Jersey 08543, USA

(Received 20 June 2007; published 31 July 2008)

Large-space-scale and long-time-scale plasma flow simulations are executed in order to study the spatial and temporal evolution of plasma parameters for two types of plasma sources used in the neutralized drift compression experiment (NDCX). The results help assess the charge neutralization conditions for ion beam compression experiments and can be employed in more sophisticated simulations, which previously neglected the dynamical evolution of the plasma. Three-dimensional simulations of a filtered cathodic-arc plasma source show the coupling efficiency of the plasma flow from the source to the drift region depends on geometrical factors. The nonuniform magnetic topology complicates the well-known general analytical considerations for evaluating guiding-center drifts, and particle-in-cell simulations provide a self-consistent evaluation of the physics in an otherwise challenging scenario. Plasma flow profiles of a ferroelectric plasma source demonstrate that the densities required for longitudinal compression experiments involving ion beams are provided over the drift length, and are in good agreement with measurements. Simulations involving azimuthally asymmetric plasma creation conditions show that symmetric profiles are nevertheless achieved at the time of peak on-axis plasma density. Also, the ferroelectric plasma expands upstream on the thermal expansion time scale, and therefore avoids the possibility of penetration into the acceleration gap and transport sections, where partial neutralization would increase the beam emittance. Future experiments on NDCX will investigate the transverse focusing of an axially compressing intense charge bunch to a sub-mm spot size with coincident focal planes using a strong final-focus solenoid. In order to fill a multi-tesla solenoid with the necessary high-density plasma for beam charge neutralization, the simulations predict that supersonically injected plasma from the low-field region will penetrate and partially fill the high-field region of the solenoid. Because of the magnetic mirroring effect, the on-axis plasma density in the solenoid depends on the injection velocity and magnetic field strength.

DOI: 10.1103/PhysRevSTAB.11.070101 PACS numbers: 52.65.−y, 52.50.Dg, 85.50.−n, 52.59.Sa

I. INTRODUCTION

Current compression of space-charge-dominated ion beams for warm dense matter and heavy ion fusion applications can be achieved by imposing an axial velocity tilt onto the beam across the acceleration gap of a linear induction accelerator, and subsequently allowing it to pass through a drift length filled with high-density plasma. In order to provide excellent space-charge and current neutralization for intense ion charge bunch compression in the neutralized drift compression experiment (NDCX) [1], numerical simulations [2,3] suggest plasma densities 10–100 times the local ion beam density throughout the drift chamber are required, thereby allowing quiescent beam propagation above the traditional space-charge limit as the beam focuses due to the head-to-tail velocity tilt [4]. The background plasma in the drift chamber for beam transport and compression experiments on NDCX is presently created using filtered cathodic-arc and barium titanate ($BaTiO_3$) ferroelectric plasma sources.

In previous simulations of the NDCX device [5–10], the full length of the drift chamber was assumed to be entirely filled with a prescribed amount of uniform and stationary high-density background plasma. Many realistic details of the plasma, such as its formation, dynamical flow to fill the drift region, and spatial and temporal profile variations, were neglected. The plasma parameters largely control the degree of neutralization of the beam space charge and current; in particular, the effectiveness of the neutralization is dependent upon the density and temperature profiles of the plasma. The upper limit of achievable ion beam current density compression increases as the available plasma density increases, especially near the focal plane.

In order to increase the understanding of techniques for creating plasma columns in beam compression experiments, assess the spatial and temporal evolution of the plasma profiles in the drift region, and provide comparisons with measurements, both types of sources are modeled in large-space-scale and long-time-scale particle-in-cell (PIC) simulations [11]. All of the PIC results presented in this paper are performed using the LSP code [3,12–14], which is a 3D parallel electromagnetic hybrid kinetic-fluid commercial code for accurately modeling dense plasmas. A reader unfamiliar with PIC numerical methods may wish to consult the general introduction to the treatment in the classic text by Birdsall and Langdon [11], as well as chapter 3 of [15]. Many of the specific methods used in the LSP code can be found in the previously mentioned references, and references therein, as well as Appendix B of [15]. The simulations in this paper solve the electro-

magnetic field equations (which require less computational time in LSP than the iterative electrostatic solver, although the electrostatic approximation would be valid in many of the cases considered), treat all particle species as explicit and kinetic, resolve the plasma frequency ω_p and cyclotron frequency Ω_c of all species, are not susceptible to the so-called plasma self-heating numerical Debye-length instability (because of an energy-conserving push) when the grid spacing size exceeds the local Debye length for a given species (the Debye lengths are mostly unresolved by the grids in the simulations presented in this paper, and this fact contributes significantly to the tractability of the 3D simulations), and use a cloud-in-cell model.

The organization of this paper is as follows. Three-dimensional simulations of the filtered cathodic-arc plasma source used in experiments to create and inject highly ionized, supersonic plasma jets into the system, in the presence of a complex magnetic field topology, are presented in Sec. II, and the coupling efficiency of the plasma flow from source to drift region is discussed. Three-dimensional PIC simulations of plasma flow from the $BaTiO_3$ ferroelectric source in a variety of symmetric and asymmetric circumstances are reported in Sec. III, and comparison to on-axis plasma density measurements is provided. In order to transversely focus an intense beam with an axial velocity tilt to a sub-mm radius coincident with the longitudinal focal plane, a strong final-focus solenoid filled with high-density plasma will be used in future experiments. In Sec. IV, simulations are carried out in order to assess the feasibility of injecting high-density plasma into a final-focus solenoid from the low-field region for beam neutralization experiments. Experiments are planned to measure whether such an injected plasma can fill the high-field region of a strong solenoid, and provide quantitative comparison to the predictions made by simulations. The dependence of beam compression on partial neutralization effects by the background plasma is studied in Sec. V, and a brief summary and discussion of the results in this paper are provided in Sec. VI.

II. FILTERED CATHODIC-ARC PLASMA SOURCE

A pair of pulsed, cathodic-arc plasma sources were initially designed and fabricated for experiments on the Neutralized Transport Experiment [16]. The filtered cathodic-arc plasma source (FCAPS) produces highly ionized *Al* plasma with supersonic ion velocities, over a density range of $n_p \sim 10^8$–10^{12} cm^{-3} and in pulse durations of 1–1000 μs, by adjusting the arc current and discharge voltage of its pulse-forming network. The cathodic-arc plasma source is of the gun variety and consists of a replaceable cathode rod surrounded by a ceramic insulator and a grounded anode [17]; it is coupled to a solenoidal coil, which can be curved up to $\pm\pi/2$ radians, serving as a macroparticle debris and neutral atom filter [18]. The macroparticle filter contributes to the externally applied magnetic field configuration responsible for manipulating the plasma parameters achieved in the experiment, such as the ion kinetic energy [19]. In general, the lack of macroparticles and neutral species is attractive for beam experiments because of the concern over charge-exchange and scattering processes. The high-current cathodic-arc source is a good choice for providing neutralizing plasma in experiments because a negligible fraction of neutral atoms and molecules will exist in the drift region. Also, such sources are easy to construct, reliable, and have long lifetimes (approximately 10^5 shots). A photograph of the FCAPS in operation on a test stand, before installation for beam compression experiments, is provided in Fig. 1 [20].

Longitudinal compression experiments require plasma densities in the $n_p \sim 10^{10}$–10^{11} cm^{-3} range, due to predictions of maximum beam density n_b provided by theory and simulations [7], whereas simultaneous transverse and longitudinal compression experiments are expected to require n_p in the range of $\sim 10^{12}$–10^{14} cm^{-3} or higher, depending on the strength of the focusing elements [8]. The FCAPS is able to produce peak n_p of $\sim 10^{12}$ cm^{-3} near the exit of the macroparticle filter region. Therefore, the plasma source may be able to provide enough plasma density for initial simultaneous focusing goals involving approximate beam radii $r_b \sim 0.2$–0.5 cm. Plasma sources capable of providing densities $n_p \gg 10^{12}$ cm^{-3} are under investigation for future experiments, which seek to increase the amount of current density compression and achieve sub-mm spot sizes.

Figure 2 illustrates the location of the cathodic-arc source in the NDCX device and provides a close-up drawing of the end of the plasma column and diagnostic box region. Two source and filter pairs are installed on opposite off-axis sides in the diagnostic box at the "downstream" end of the experiment (relative to the direction of beam propagation) and positioned to face the "upstream" direc-

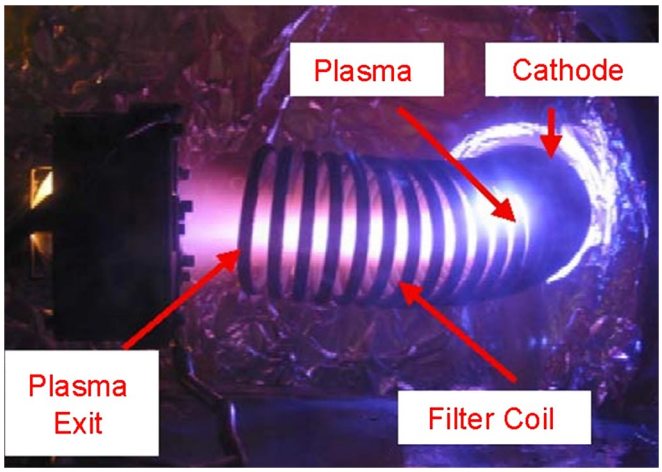

FIG. 1. (Color) Photograph of the FCAPS in operation on a test stand, before installation on the NDCX device [20].

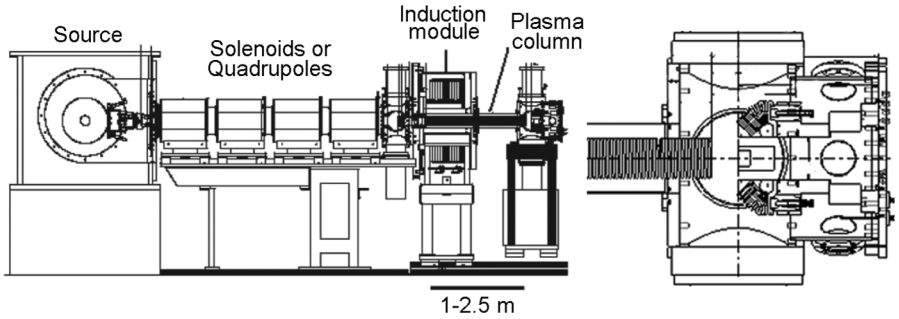

FIG. 2. Schematic of the NDCX device (left) and close-up drawing of the end of the plasma column and diagnostic box region (right). The two cathodic-arc source filter coils are angled at $\theta = \pm\pi/4$ radians relative to the guide solenoid. The drift tube and guide solenoid can extend from 1–2.5 m.

tion. The pairs need to be placed out of the beam line line-of-sight in order to avoid interacting with the beam, as well as accommodate beam diagnostics. High-density plasma is created at vacuum arc cathode spots [21] on the surfaces of the *Al* sources.

Magnetic fields provided by the two curved filter coils assist in the upstream injection of plasma by guiding it into the beam line from the two off-axis locations downstream of the drift chamber. The curved magnetic fields of the bent filter coils cause only ionized metal plasma to symmetrically reach the neutralization region. In the configuration considered here, the filter coils are placed at angles of $\pm\pi/4$ radians relative to a long axial guide solenoid. In order to fill the variable 1–2.5 m high-density plasma column, a solenoidal magnetic field of the same length is required in the drift region in order to provide confinement of the plasma flow. The presence of the guide field also influences beam particle trajectories, as well as neutralization physics, by constraining the electron motion. The fringe fields of the filter coils and guide solenoid overlap and enable the transfer of plasma from the sources to the drift region. Plasma streams into the beam line and the ion species can attain tens to a few hundred eV in directed energy, with a typical range of ion drift velocities around $0.5\text{–}3 \times 10^4$ m s^{-1} [19]. A one-dimensional model of a single cathode spot and the resulting plasma jet ascribe the acceleration of the ions to the electron pressure gradient acting through electron-ion friction [22].

The main drawback to the described method of providing the high-volume plasma is the injection method. Both an electrostatic trap and a magnetic dipole are necessary to reduce the upstream movement of the plasma beyond the drift region. If the upstream motion of the plasma is insufficiently stopped and electrons are allowed to penetrate into the acceleration gap or magnetic transport regions, the emittance of the beam can increase due to partial neutralization effects, resulting in degradation of the focal spot and pulse length. Active research studies whether cathodic-arc plasma can penetrate into the regions intended for unneutralized beam transport. Other sources of secondary electrons and electron clouds, such as halo beam ion impact on the chamber walls [23] in the aperture and magnetic transport regions, are under active investigation in order to mitigate their role in beam compression experiments [24].

Guidance for designing the cathodic-arc plasma source to achieve high plasma density n_p in the drift region, and to understand plasma flows in complex magnetic geometries, is provided with large-space-scale and long-time-scale plasma flow PIC simulations [15]. Parameters that affect the coupling efficiency of the plasma from the sources to the drift region include the arc voltage and cathode material, the angle θ of the filter coils relative to the guide solenoid, the horizontal separation distance d between the end of the guide solenoid and midplane exit of the filter coils, the offset h of the midplane exit of the filter coils from the beam line axis, the magnetic field magnitudes provided by the filter coils and guide solenoid currents, and the relative ratio r of the peak magnetic field strengths between the guide solenoid and filter coils. A calculation from an analytical model that calculates the magnetic field topology using finite-length solenoid expansions in the transition region between the three solenoids (which share a plane) is presented in Fig. 3, in order to illustrate the various parameters. Both the analytical and PIC models consider the full 3D problem due to the lack of symmetry in any coordinate. In the case shown in Fig. 3, the inner radii of the filter coils and guide solenoid are $r_f = 2.5$ cm and $r_g = 3$ cm, respectively, the offset $h = \pm 6$ cm, and the angle $\theta = \pm\pi/4$.

Shorter separation distances d result in higher fields in the transition region because of the increased overlap of fringe fields. Reduced filter coil angles θ also help improve the plasma flow line-of-sight to the guide solenoid, but reduce the offset height and decrease the clearance for the beam and its diagnostics. Experiments show that stronger magnetic fields can increase plasma temperatures T_p and reduce density gradients compared to free expansion [19]; also, different magnetic field geometries may increase or decrease the kinetic energy of the plasma ions. The absolute values and relative ratio r of peak magnetic field strengths in the guide solenoid and filter coils are important

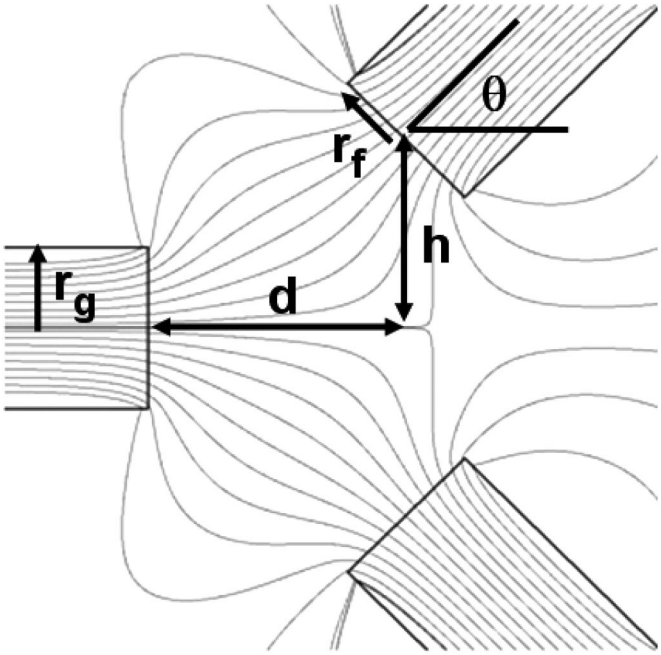

FIG. 3. Analytical calculation of magnetic field lines from three finite-length solenoids, corresponding to a $d = 8$ cm, $h = \pm 6$ cm, and $\theta = \pm\pi/4$ configuration for FCAPS injection into the NDCX beam line (a slice through the midplane is shown). The peak magnetic fields within the filter coils and guide solenoid are each 2 kG (corresponding to $r = 1$).

to consider in terms of plasma steering because of the effects of ∇B and curvature drifts, as well as the role of magnetic mirroring [25].

Optimization of the plasma density magnitude and uniformity in the drift length involves the proper relative placement and orientation of the filter coils, finding the appropriate combination of magnetic field strengths, and ensuring an adequate amount of plasma fill in the guide solenoid. In addition, the plasma ion kinetic energies can be manipulated by the magnetic field configuration [19]. The plasma flow profiles within a particular field topology can be assessed using LSP simulations and provide insight into the coupling efficiency of the off-axis plasma sources to the axial neutralization section. PIC simulations offer an increased understanding of plasma flow in complicated magnetic field topologies, where other theories and methods may be inadequate or intractable, and help determine the optimum configuration.

The goal of the FCAPS numerical simulations is to study the coupling efficiency of the plasma flow after creation, through the curved filter coils, and into the guide solenoid where beam neutralization occurs. A diagram of the LSP simulation setup, which closely resembles the NDCX device configuration, is shown in Fig. 4. Three-dimensional Cartesian coordinates are used over $x = \{-5$ cm, $+5$ cm$\}$, $y = \{-8$ cm, $+10$ cm$\}$, and $z = \{-12$ cm, $+12$ cm$\}$. The beam travels in the $-\hat{y}$ direction in this system, aligned on the $z = 0$ axis. Recall that the plasma injection occurs at the downstream end, and the intended focal plane is near $y = 0$.

The 3D magnetic fields from static current flow through the three solenoids corresponding to the case in Fig. 3 are calculated (with curved filter coils) [26] using the finite-element code VECTOR FIELDS OPERA-3D [27]. The geometry includes the offset $h = \pm 6$ cm, angle $\theta = \pm\pi/4$, and separation distance $d = 8$ cm. The relative ratio of peak magnetic field strengths between the guide solenoid and filter coils is $r = 1$, with an absolute peak magnitude of

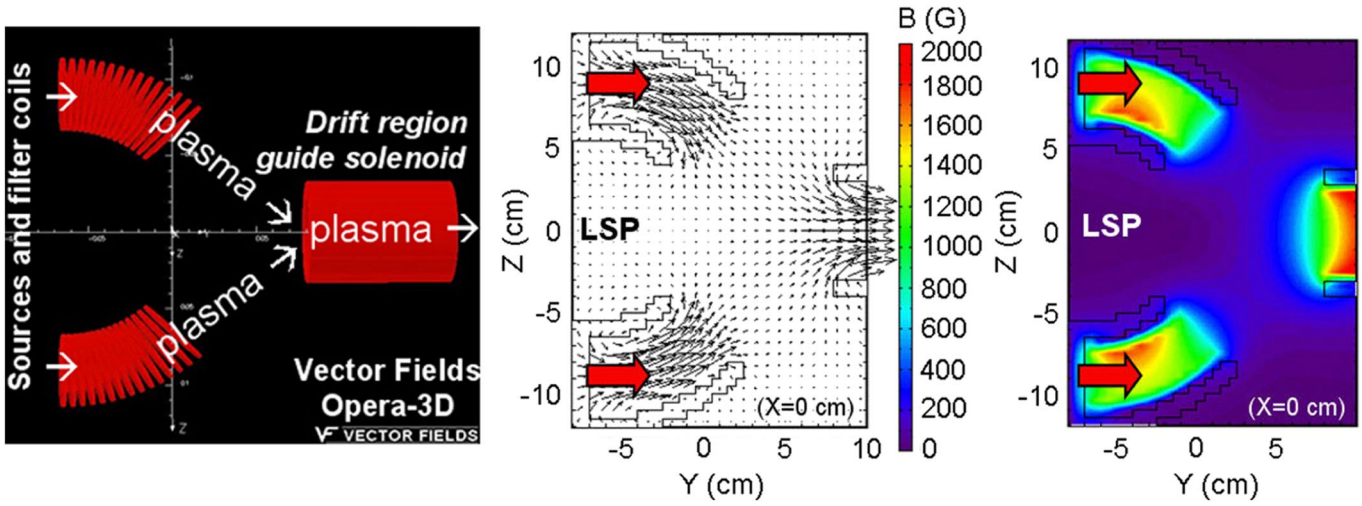

FIG. 4. (Color) Schematic and magnetic field topology from the FCAPS simulation (slices through the $x = 0$ cm midplane are shown). Magnetic fields corresponding to the case in Fig. 3 (with curved filter coils) are calculated [26] by VECTOR FIELDS OPERA-3D [27] from the solenoid arrangement (left), and the resulting vector field (middle) and isocontours of total field magnitude (right) are initialized into the LSP code. White and red arrows show the intended plasma flow and location of the sources, respectively. The focal plane is near $y = 0$.

$B_z = 2$ kG within them. Figure 4 also presents the resulting vector field and isocontours of total field magnitude initialized in the LSP code. Since the simulation is conducted in 3D and the computation time increases with the number of grid nodes, the spatial resolution in each direction is limited to 0.5 cm. Conducting boundary conditions are imposed at the walls of all the solenoids and along the outer boundary of the entire simulation domain. Once plasma enters the guide solenoid of radius $r_g = 3$ cm at the $z = 0$ plane, it is absorbed by the simulation boundary at the $y = +10$ cm plane, but would flow upstream for 1–2.5 m from that location to form the plasma column in an experiment.

Initially, the simulation begins as an empty space with the imposed background magnetic field topology and boundary conditions, but without particles, according to Fig. 4. Plasma is continually injected from the base of the filter coils in the direction indicated beginning at $t = 0$, until steady-state flow is observed. The simulated ions are injected from the base of the two bent filter coils of radius $r_f = 2.5$ cm at $y = -7$ cm and $z = \pm 9$ cm, with an ion velocity v_i in the $+\hat{y}$ direction of 1.44 cm μs^{-1} ($E_i \sim 29$ eV for Al^+), in agreement with experimental measurements [19,20]. At the two plasma jet injection locations, the supersonic ion velocity is parallel to the magnetic field. The peak ion current density is approximately $J_{\mathrm{pi}} \sim 40$ mA cm^{-2} (an equal amount of electron current density is also injected), corresponding to a peak plasma density estimate of $n_p \sim 2 \times 10^{11}$ cm^{-3} near the sources within the filter coils. Maxwellian distributions with temperatures $T_i = 1$ eV and $T_e = 5$ eV are imposed on the injected ion and electron populations, respectively. The injected ion Mach number ($M_i \equiv v_i/C_s$, where the sound speed C_s includes the T_i correction, $C_s = \sqrt{(T_e + \gamma T_i)/M_i}$) is approximately 2.7. The simulation is executed to $t = 40$ μs with a time step satisfying the constraints $\omega_{pe}^{\mathrm{peak}} \Delta t < 0.75$ and $\omega_{ce}^{\mathrm{peak}} \Delta t < 1$ (about 1.33×10^6 total steps), where $\omega_{pe}^{\mathrm{peak}}$ and $\omega_{ce}^{\mathrm{peak}}$ are the peak expected electron plasma and cyclotron frequencies, respectively. During steady-state plasma flow, more than 5×10^5 particles are explicitly pushed on the simulation grid at each time step. It should be noted that the plasma injection described in this simulation is only an approximate model, since the actual plasma creation mechanism itself is not included; the correct integrated modeling of the surface physics and source distribution during plasma creation within the sources would be cumbersome and is beyond the scope of this paper, but could impact the results.

Generally, the complex magnetic topology in the entire region affects the plasma flow profiles, including near the sources, where it influences the discharge and plasma properties. Not only does the relative field strength r affect the plasma phase space, but the intervening gradients do as well. In the configuration here, the ions are unmagnetized with gyroradii ($\rho_L = v_\perp/\omega_c$) on the system scale size (cm), whereas the electrons are magnetized (μm). Therefore, the electrons mostly follow field lines and ambipolar forces (defined as the electric force arising from the gradient of the ambipolar potential) influence ion movement. The range of betas (ratio of plasma pressure to magnetic pressure) considered are very small, of order 10^{-3} to 10^{-5}. It should also be noted that the noniterative electromagnetic field solver in LSP is used for reasons of computation speed, compared to the iterative electrostatic solver, although the electrostatic approximation is appropriate in these simulations and is expected to yield similar results.

Figure 5 illustrates plasma densities at various times in the form of 2D $\{y, z\}$ and $\{x, z\}$ isocontours through different planes. The fastest ions of the Al^+ plasma that are accelerated by an electron sheath in the $+\hat{y}$ direction during the initial expansion, do not couple well to the guide solenoid because of their high average energies, and instead strike the diagnostic box at $x^2 + z^2 > 9$ cm^2 at $y = +10$ cm. Subsequent ions are not accelerated and the simulation space fills with plasma. As ions exit the top (bottom) filter coil, they begin to turn with the magnetic field and gain average directed energies in the $-\hat{z}$ ($+\hat{z}$) and $-\hat{x}$ ($+\hat{x}$) directions of approximately $E_i \sim 5$ eV and $E_i \sim 3.5$ eV, respectively, at the expense of 8.5 eV from the initial $E_i \sim 29$ eV in the $+\hat{y}$ direction. Electrostatic sheaths are quickly established near the conducting boundaries of the filter coils to decrease the preferential electron loss near those boundaries. After exiting the filter coils, the plasma expands into the intermediate region of decreased magnetic field strength before encountering an increasing field strength region near the guide solenoid. The density drops the most near the exit of the filter coil due to the expansion into the low-field region. By $t = 8$ μs, $n_p > 10^9$ cm^{-3} begins to fill the $z = 0$ axis region within the guide solenoid.

The initial plasma expansion into the space ceases around $t \sim 20$ μs, when steady-state conditions begin. The density in the center of the guide solenoid is shown to exceed 1.5×10^{10} cm^{-3} (recall that the initial $n_p \sim 2 \times 10^{11}$ cm^{-3} in the filter coils). As shown in Fig. 6, approximately 50% of the plasma that reaches the $y = +9.5$ cm plane is coupled into the guide solenoid, although the overall coupling efficiency of the plasma density from the sources to the guide solenoid is approximately 8%. Also, both plasma jets overlap near the $y = +9.5$ cm plane, and nearly equal populations of particles moving in the transverse $\pm\hat{x}$ and $\pm\hat{z}$ directions exist there. After steady state is reached, the $+\hat{y}$-directed average ion energy into the guide solenoid is $E_i \sim 19$ eV. The 10 eV difference compared to the initial energy is coupled through the field configuration into motion in the other two directions. Obviously, at least some of this energy transfer is necessary in order to divert the plasma created off-axis onto the $z = 0$ axis.

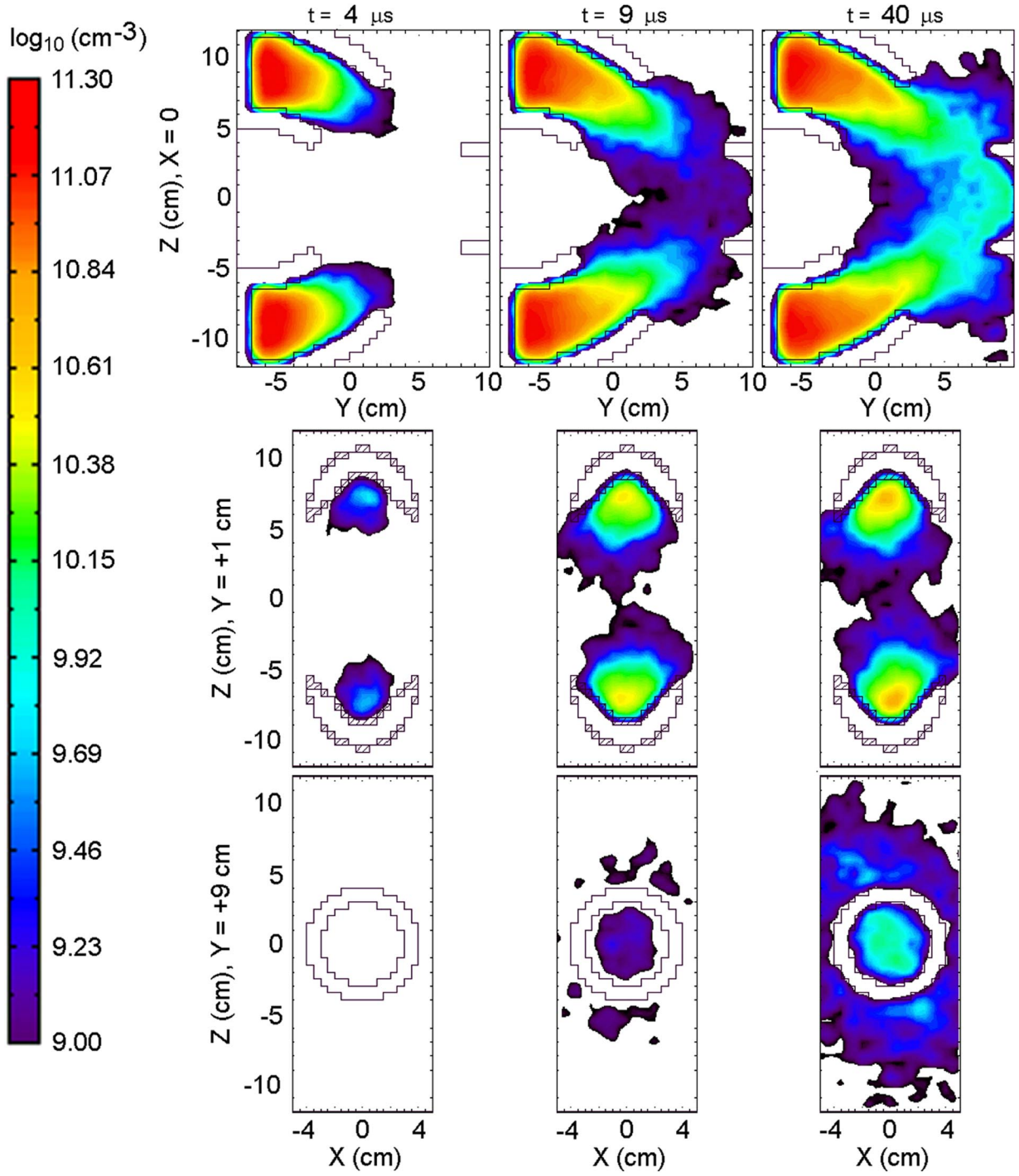

FIG. 5. (Color) FCAPS plasma density n_p isocontours at $t = 4$ μs (left column), $t = 9$ μs (center column), and $t = 40$ μs (right column) as $\{y, z\}$ slices at $x = 0$ (first row), $\{x, z\}$ slices at $y = +1$ cm (second row), and $\{x, z\}$ slices at $y = +9$ cm (third row). All plots are on the same $\log_{10}$ scale.

Magnetic field gradients perpendicular and parallel to the unit vector of the magnetic field $\hat{\mathbf{b}} = \mathbf{B}/B$ are present in the FCAPS injection configuration, as well as field curvature. Guiding-center electron drifts across the magnetic field, acceleration and deceleration along the magnetic field, and ambipolar forces are expected to play a role in the ion dynamics. Plasma ∇B and curvature (of locally constant B) drifts affecting the first-order electron particle motion are important in this scenario, since they affect the coupling efficiency of plasma into the guide solenoid. As the magnetized species, the electrons acquire perpendicular (to $\hat{\mathbf{b}}$) guiding-center drift velocities from the nonuni-

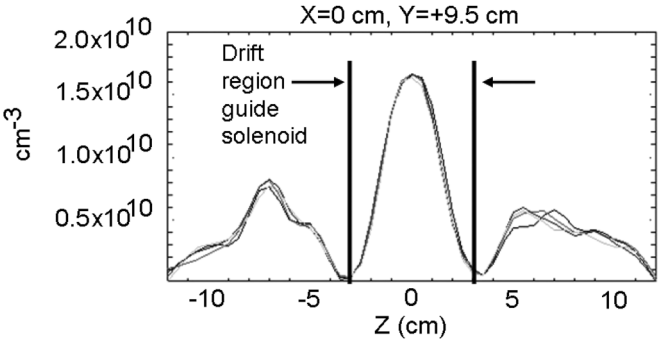

FIG. 6. Axial slices of plasma density n_p at late times ($t =$ 35–40 μs) at $x = 0$ and $y = +9.5$ cm. Steady-state profiles begin at $t \sim 20$ μs. Of the plasma that reaches $y = +9.5$ cm, ~50% has been coupled into the guide solenoid.

form magnetic fields according to [25]

$$\mathbf{v}_d = -\frac{W_\perp}{e_c}\frac{\mathbf{B}\times\nabla B}{B^3} - \frac{2W_\parallel}{e_c}\frac{\mathbf{B}\times(\hat{\mathbf{b}}\cdot\nabla)\hat{\mathbf{b}}}{B^2}, \quad (1)$$

where e_c is the electron charge, and $W_\perp$ and $W_\parallel$ are the average perpendicular and parallel particle energies relative to the applied magnetic field, respectively. Magnetized particles traveling in a curved magnetic field experience an outward centrifugal pseudoforce, $\mathbf{F}_{\rm cf} = mv_\parallel^2\mathbf{R}_c/R_c^2$, where R_c is the radius of curvature vector [25]. Figure 5 shows electron guiding-center drifts in the $-\hat{x}$ ($+\hat{x}$) direction and centrifugal pseudoforces affecting plasma injected from the top (bottom) filter coil. However, the radius of curvature changes polarity from the filter coils to the guide solenoid, resulting in the offsetting of some of the drift motion. The analytical evaluation of perpendicular $v_\perp$ and parallel $v_\parallel$ velocities relative to the local $\hat{\mathbf{b}}$ in this nonuniform magnetic topology would be complex. Indeed, due to the orientation of the three solenoids, some of the $v_\perp$ in the filter coils is actually $v_\parallel$ relative to the guide solenoid and vice versa. Competing effects, like the reduction of ∇n_p and variation in drifts, imply that the ion velocity, which responds to ambipolar forces as a function of relative and absolute field strengths, will exhibit nonmonotonic behavior. Experimental evidence affirming this conjecture and additional related details are provided in [19].

Magnetic field gradients parallel to $\hat{\mathbf{b}}$ are unavoidable in such an injection configuration, and careful evaluation of the parallel velocity dynamics of magnetized species are required because of forces arising in the direction opposite to the field gradients. The magnetic moment of a charged particle, $\mu = mv_\perp^2/2B$, is an adiabatic invariant in the limit of no collisions. The conservation of μ in the presence of a ∇B along $\hat{\mathbf{b}}$ leads to a well-known result called the magnetic mirror effect [28]. Conservation of a charged particle's total kinetic energy W implies that the $v_\parallel$ will increase or decrease if the field strength decreases or increases along the field line, respectively. In the absence of electric fields and collisions, two constants of the motion (W and μ) ensure that $v_\parallel$ changes with B according to $mv_\parallel^2/2 = W - \mu B$ [25].

Because of magnetic mirroring, plasma streaming out of (into) the filter coils (guide solenoid) is expected to accelerate (decelerate) along $\hat{\mathbf{b}}$, in general, due to the force arising in the direction opposite to the field gradient, $\mathbf{F}_\parallel = -\mu\nabla B$. The effect is relatively minor in this case because of the supersonic nature of the injected ions and relative ratio $r = 1$ of the field strengths. Figure 5 demonstrates that only a small fraction of the plasma is reflected away from the guide solenoid, and the substantial majority of it is able to penetrate into the drift region. If the magnetic field of the guide solenoid were much stronger and the ions were not supersonic, the amount of plasma able to penetrate into the drift region would be reduced. Simulations involving much stronger solenoidal fields, where mirroring effects dominate the plasma-fill dynamics, will be discussed in Sec. IV.

The presence of the magnetic field and ambipolar forces increases the temperature T_p relative to free expansion without a field, and decreases the corresponding plasma density gradient ∇n_p along the field, whereas the density gradient across the field is increased. For this reason, the quantitative plasma dynamics are configuration dependent. As the plasma expands along field lines and down the magnetic field gradient provided by the filter coils, the n_p and electron temperature T_e drop, while the ion temperature is ill defined because of anisotropy. An electron temperature drop from $T_e = 5$ eV to $T_e = 1$–2 eV is typically observed in cathodic-arc plasma source experiments and theoretical models [19], and a decrease from $T_e =$ 5 eV to $T_e = 2$–3 eV is observed in these simulations (where T is reported as $\frac{2}{3}E_{\rm average}$). Figure 7 shows the T_e isocontours in the $x = 0$ plane from the previously discussed simulation and provides comparison to an increased initial $T_e = 10$ eV simulation; the results are very similar when the factor of 2 is taken into account. Three additional simulations consider injected temperature pairs of $T_i = 1$, 3, and 10 eV with $T_e = 5$, 10, and 20 eV, respectively, and result in small ($< 20\%$) differences between n_p profiles and coupling efficiencies. The ion Mach numbers are approximately 2.65, 1.72, and 1.06, respectively, where higher coupling efficiencies and plasma densities are associated with larger Mach numbers and lower temperatures.

Filtered cathodic-arc plasma sources typically create a range of ion charge states, but the effect has been neglected in the present simulations. Velocity measurements [29] demonstrate the effective independence of v_i (and E_i) from the charge state, implying that the singly ionized Al^+ simulation presented here is generally valid. Consequently, the acceleration mechanism near the source is assumed to be hydrodynamic in nature, and not associated with an electric field from a change in potential. The presence of the macroparticle filter's magnetic field is

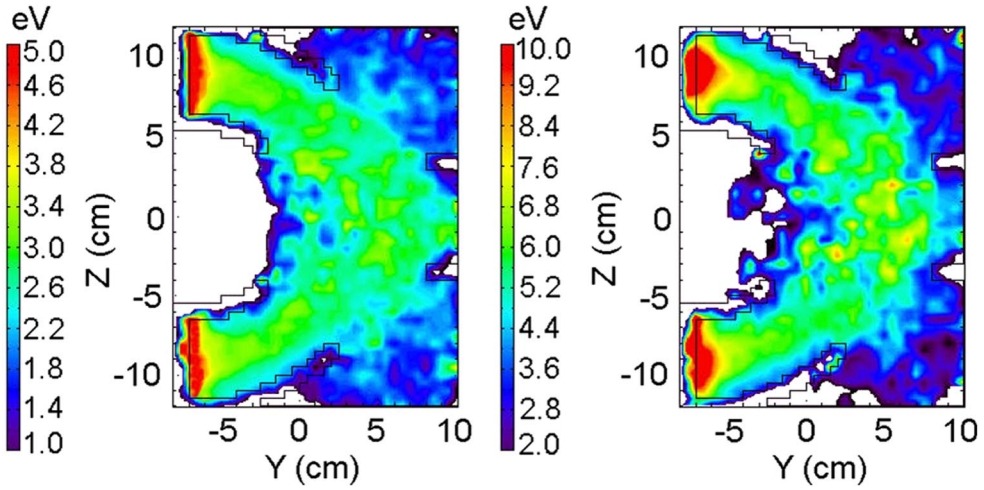

FIG. 7. (Color) T_e isocontours during steady-state FCAPS injection, presented as $\{y, z\}$ slices at $x = 0$. T_e decreases by a factor of 2 from inside the filter coils to the guide solenoid in the cases of initial $T_e = 5$ eV (left) and $T_e = 10$ eV (right).

also known to directly increase the ion charge state of the cathodic-arc source [19]. The densities n_p used in these FCAPS injection simulations are estimated to be a factor of 5–10 lower than the expected peak values achievable in the experiment ($n_p \sim 10^{12}$ cm^{-3}), due to the desire to relax the numerical time step requirement of resolving the electron plasma frequency time scale. However, the nominal operating regime of the FCAPS for early longitudinal compression experiments was approximately the same ($n_p \sim$ few 10^{10} cm^{-3}, with $T_p \sim 3$ eV).

The main conclusion of this section is that the simulations provide evidence for significant n_p loss in the filter coils due to a combination of electron curvature drifts and acceleration of plasma electrons away from the high-field region due to the field gradient. Steps can be taken to increase the plasma density coupling efficiency into the drift region guide solenoid for future beam compression experiments. Reducing the macroparticle filter angle $\theta = \pm\pi/4$ has the effect of increasing the transported plasma density to the $z = 0$ axis, but may also increase the neutral and macroparticle debris population. Densities can be further enhanced by increasing the arc current and discharge voltage, increasing the number of sources beyond two, and positioning the filter coils closer to the guide solenoid. A wide range of n_p can be chosen for beam experiments by judicious choice of the parameters involved in the plasma injection, including the timing of the beam arrival in the drift length. Further plasma density optimization of the coupling efficiency from the sources to the guide solenoid is possible using the numerical simulation technique outlined here.

III. FERROELECTRIC PLASMA SOURCE

Another large-volume plasma source involves a design based upon the use of ferroelectric materials [30], which can be used as large-surface-area electron emitters capable of producing high current densities [31,32]. The principle of operation for a plasma source made of ferroelectric ceramic relies on large dielectric constants to amplify local surface electric fields. Ferroelectric materials in common use as plasma sources typically have dielectric constants anywhere from $\epsilon_r \sim$ 1000–6000; barium titanate ($BaTiO_3$, $\epsilon_r \sim$ 1000–3000) was selected for development into a plasma source for the NDCX device due to its durability and cost. Earlier plasma source research [33,34] for intense beam compression experiments developed a ferroelectric plasma source (FEPS) constructed from lead zirconium titanate [Pb(Zr, Ti)O_3, $\epsilon_r \sim$ 3000–6000]. However, a shift to $BaTiO_3$ was made due to its increased robustness, as well as lack of creating lead-containing dust [35].

The main advantage of the ferroelectric source is found in the method by which plasma fills the drift length. In contrast to the FCAPS injection method, the cylindrical FEPS does not use a magnetic guide field. Instead, the source radially fills the chamber with plasma created at the wall radius. The long solenoid that guides cathodic-arc plasma to an electrostatic trap and magnetic dipole, and affects beam trajectories and neutralization processes, is unnecessary. Finally, the length and voltage of the ferroelectric source can be designed to consume less power and operate at lower neutral pressures ($p_n \sim 10^{-5}$–10^{-6} Torr), since the source can be tailored to make high-density plasma only where needed in experiments, resulting in a power consumption advantage and helping to prevent charge-exchange or stripping processes involving beam ions compared to other sources.

In order to develop a large-volume and high-density source of plasma, a ferroelectric material is placed between a rear continuous electrode and a front wire electrode. The dielectric is in contact with the rear electrode, whereas a ''microgap'' spacing exists between the dielectric surface and the front electrode. An applied bias (4–7 kV) pulsed into the rear electrode produces a large electric field nor-

mal to the dielectric material, creating an electron avalanche and surface plasma in the microgap comprised of the ferroelectric ceramic itself [36]. Pointlike explosions of plasma are expelled from the ceramic and accelerated past the front electrode.

To make an arbitrarily long cylindrical source (in the axial direction) useful for beam neutralization experiments, the ferroelectric material is formed into a ring with an inner diameter of $D_r = 7.62$ cm, and each modular ring is $\Delta z_r = 3.7$ cm long in the axial direction [35]. The design allows for rings to be stacked, forming a cylindrical FEPS of arbitrary length with fixed diameter. The rear (outer) electrode receives the high-voltage bias and is formed by a solid wrapping of copper; the front (inner) electrode is created with a metallic mesh. Such a plasma source, about $L = 85$ cm in length, has been developed at the Princeton Plasma Physics Laboratory for use in the NDCX device. Four axial ports, consisting of $z_p = 5$ cm-long Delrin rings with two diametrically opposite holes of diameter $D_p = 2.54$ cm, are included for transverse diagnostic access; plasma is not created in these "gap" regions, which divide the source into modular subsegments of $\Delta z \sim 15$–18 cm. After the high-voltage and high-current (~ 1.2 kA peak) pulse passes into the device, the chamber is then filled over the course of 3–9 μs with plasma. The relative timing of the plasma source pulse and ion beam injection in experiments is configured so that peak plasma density n_p is present as the beam passes through the column of plasma, in order to ensure the highest levels of plasma neutralization are available for the compressing beam. Plasma conditions can be controlled by adjusting the parameters of the applied high-voltage pulse.

The ferroelectric source was designed, assembled, tested, and characterized before integration into the NDCX device. Figure 8 contains two photographs of the plasma source. In order to sufficiently neutralize intense ion beams, numerical simulations of longitudinal compression experiments demonstrate the need to provide plasma densities of approximately $n_p \sim 10^{10}$ cm^{-3} [37]. The $BaTiO_3$ source was originally envisioned to replace the FCAPS (from Sec. II) in the main drift region, due to a number of advantages. However, upcoming simultaneous transverse and longitudinal focusing experiments planned for NDCX are expected to require $n_p \geq 10^{12}$ cm^{-3} near the focal plane. Therefore, both plasma sources are planned for utilization in tandem, with the FEPS providing sufficient plasma density throughout the first 85 cm of the drift region. The FCAPS will be employed near the simultaneous focal plane, where larger n_p will be available for the additional neutralization required by the larger beam densities n_b.

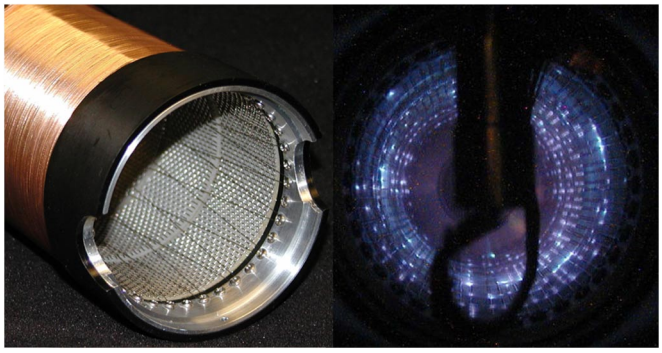

FIG. 8. (Color) Photograph of the $BaTiO_3$ FEPS (left) and open-shutter exposure of the source in operation (right). Plasma is created near the points where the front (inner) mesh electrode is near the surface of dielectric material.

The ferroelectric plasma source is modeled in large-space-scale and long-time-scale PIC simulations [15]. The goals of the numerical simulations are to investigate: (1) how the volume fills with high-density plasma; (2) how the plasma profiles evolve with time inside of the source; and (3) whether nonuniform plasma creation affects the plasma production (both axial and azimuthal asymmetry in creation conditions). In order to study asymmetric plasma creation and flow, the $BaTiO_3$ source simulations are carried out in 3D. Axially asymmetric plasma formation occurs due to the presence of transverse diagnostic access ports, which do not create plasma; azimuthally asymmetric plasma formation is observed experimentally by noting that the emitted radiation is not uniform along each segment's walls.

Figure 9 provides a schematic of the 3D simulation space setup in the LSP code. Cylindrical coordinates are employed, and periodic boundary conditions are imposed in both the θ and z directions. The $\{r, \theta, z\}$ simulation grid extends from $r = 0$ to $r = 4$ cm, $\theta = 0$ to $\theta = 2\pi$, and $z = 0$ to $z = 25$ cm, with a spatial resolution of $\Delta r = 0.1$ cm, $\Delta\theta = 0.196$ radians, and $\Delta z = 0.5$ cm. Conducting boundaries are assumed at the wall $r_w = 3.8$ cm (the front/inner electrode is ground), and a transverse access port of $\Delta z = 5$ cm is included in between two $\Delta z = 10$ cm-long regions of plasma formation. The actual plasma source consists of four such units in series with four ports. Because of the periodic axial boundary conditions, the ends of the actual FEPS are not modeled in this simulation.

It should be noted that the exact composition of the ferroelectric ceramic (and plasma) is not known, due to the manufacturer's nondisclosure of material development methods. Laboratory tests to identify the elements present in dust after operation revealed many elements, and so the plasma ions are most likely a mix of several species and molecules. In order to determine the effective mass m_i^{eff} of the ion population, several simulations are executed and compared to measurements. As will be discussed later, an effective $m_i^{\text{eff}} = 3 \times$ Ba, which is heavier than the mass of $BaTiO_3$, is observed to agree well with measurements of the on-axis plasma density $n_p(t)$.

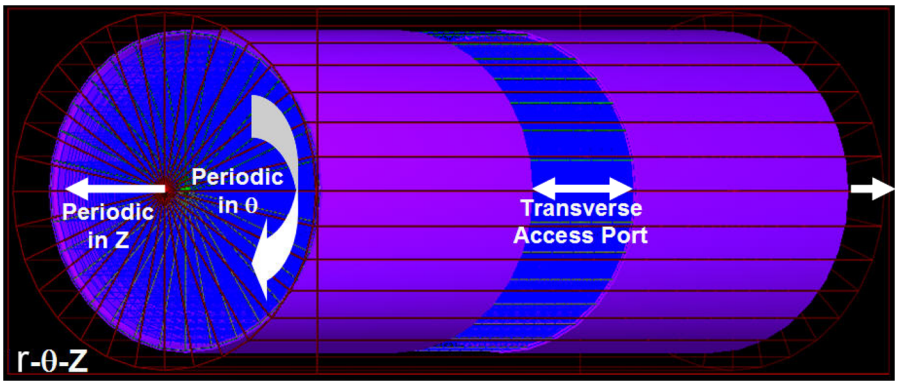

FIG. 9. (Color) Simulation space setup of the 3D ferroelectric source in the LSP code. The regions where plasma is produced are indicated by purple cylindrical shells.

Langmuir probe measurements [34] indicate that the source discharge current is proportional to n_p. Therefore, the temporal current density of the injected ions $J_r^i(t)$ in the simulation is assumed to be proportional to the measured load current of the source, as shown in Fig. 10. When J_r^i returns to zero, no additional particles are injected. Also, the temporal injection velocity of the ions $v_r^i(t)$ in simulation is assumed to be proportional to the load voltage, since the latter determines the electric field in the dielectric and near the microgap. The proportionality constants were chosen so that the resulting $n^i(t) \sim J_r^i(t)/v_r^i(t)$ approximately reproduced the experimental on-axis plasma density $n_p(t)$ (the constants were approximately equal and estimated to be $\sim 0.01 \pm 0.005$). The plasma particles are injected in the $-\hat{r}$ direction from the two $\Delta z = 10$ cm regions of plasma creation at $r_w = 3.8$ cm, over the full $\Delta\theta = 2\pi$ azimuth, and with imposed Maxwellian temperatures $T_e = T_i = 20$ eV. The average electron temperature is measured to be $T_e \sim 20$ eV at the time of peak n_p, and good comparison is found between simulation and experiment when the ions are initialized with the same temperature. The peak injection $J_r^i = -10$ mA cm^{-2} and $v_r^i = -0.375$ cm μs^{-1}, which corresponds to approximately $E_i \sim 30$ eV. Neutrals and collisions are not included. The constituencies of neutral populations are presently not diagnosed well in experiments, and the plasma densities are presently too low in the ferroelectric source for charged particle collisions to be important. The injection model does not include the plasma creation mechanism itself.

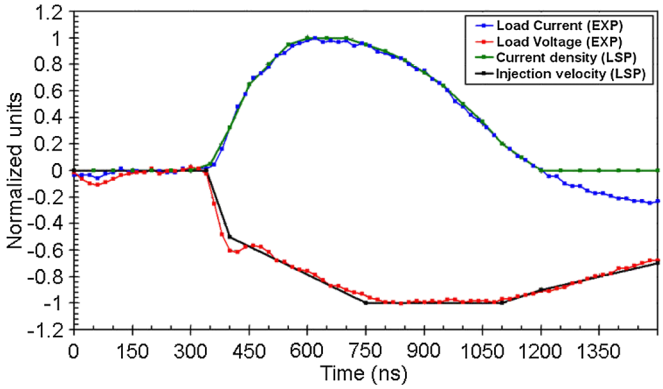

FIG. 10. (Color) Input parameters used in PIC simulation for the injected ion species in the ferroelectric source. The peak current density is $J_r^i = -10$ mA cm^{-2}, and the peak radial injection velocity is $v_r^i = -0.375$ cm μs^{-1}.

The simulation is executed to $t = 20$ μs with a time step of $\omega_{pe}^{\text{peak}} \Delta t < 0.2$ (about 8×10^5 total steps). The maximum total amount of particles explicitly pushed on the simulation grid in one time step reaches approximately 2.3×10^7 at $t \sim 4.5$ μs. Early in time ($t < 3.5$ μs), a sheath accelerates most of the subsonic plasma ions, and facilitates rapid expansion towards $r = 0$, with the fast ions of the initial expansion causing large average kinetic energies to arrive at $r = 0$ first. Figure 11 plots the plasma density obtained at various times in the form of radial slices through $\theta = \pi$ and 2D $\{r, \theta\}$ isocontours through the midplane of one of the two plasma-creating ceramic segments. The small residual asymmetries evident in Fig. 11 are consistent with increasing particle noise near the $r = 0$ axis. The density in the core is shown to exceed $n_p \sim 10^{10}$ cm^{-3} by $t = 4.7$ μs, and peaks on-axis at $n_p \sim 2.5 \times 10^{10}$ cm^{-3} around $t = 6$ μs. At that time, nearly equal ion populations moving in the $\pm\hat{r}$ directions exist near $r = 0$, with an average $E_i \sim 30$ eV. The plasma persists in the chamber above the $n_p \sim 10^{10}$ cm^{-3} level until $t = 11$ μs. Azimuthal profile symmetry is maintained throughout the simulation, as shown in Fig. 11.

Figure 12 shows the plasma density n_p obtained at various times in the form of axial slices through the $r = 0$ axis, and 2D $\{r, z\}$ isocontours through $\theta = \pi$. Of importance for beam experiments is whether the $\Delta z = 5$ cm gaps from the transverse diagnostic ports become filled with sufficient on-axis n_p in order to maintain good charge neutralization of the beam. The density in the axial gap is shown to exceed $n_p \sim 10^9$ cm^{-3} by $t = 5$ μs and peaks in the gap's center at $n_p \sim 4 \times 10^9$ cm^{-3} around $t = 6.8$ μs,

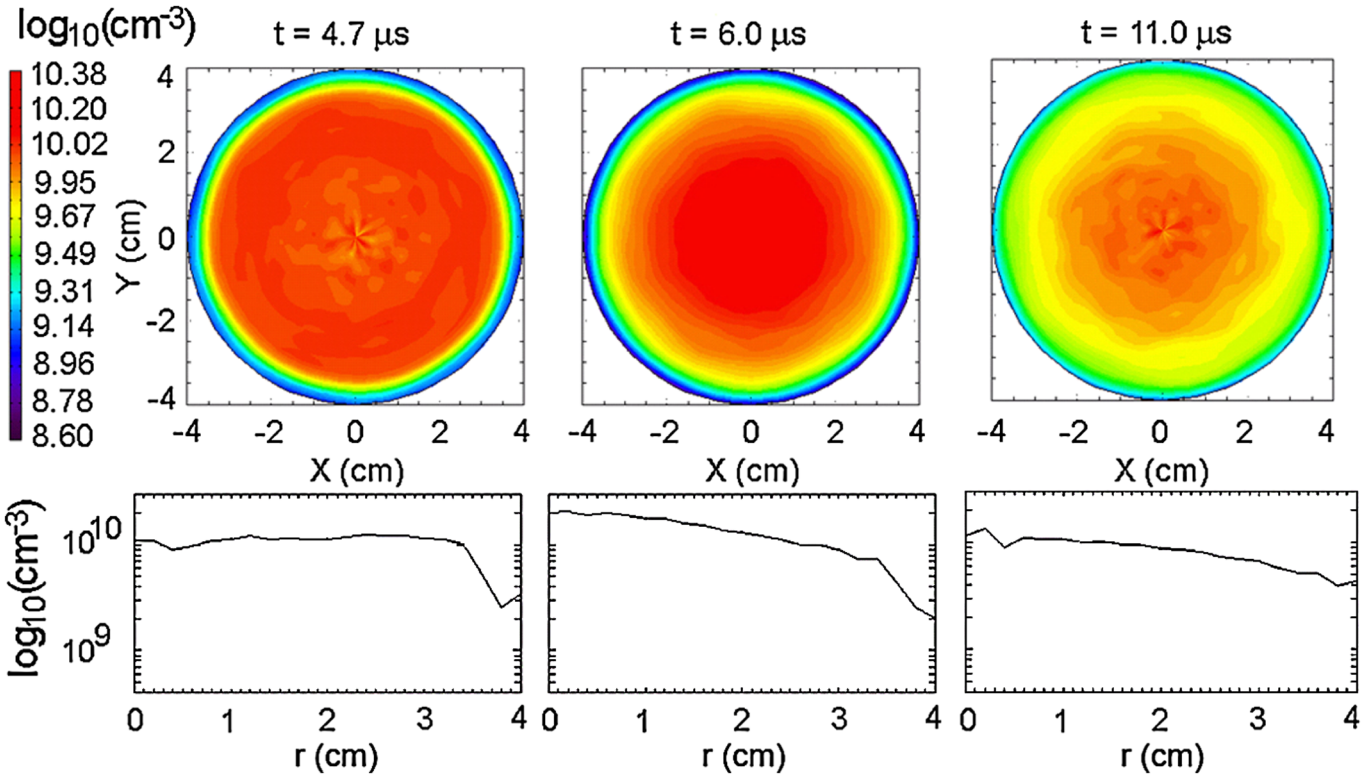

FIG. 11. (Color) n_p radial slices at $\theta = \pi$ (bottom) and $\{r, \theta\}$ isocontours (top) through the midplane of a ferroelectric ceramic segment at $t = 4.7$ μs (left), $t = 6$ μs (center), and $t = 11$ μs (right). All plots are on the same $\log_{10}$ scale.

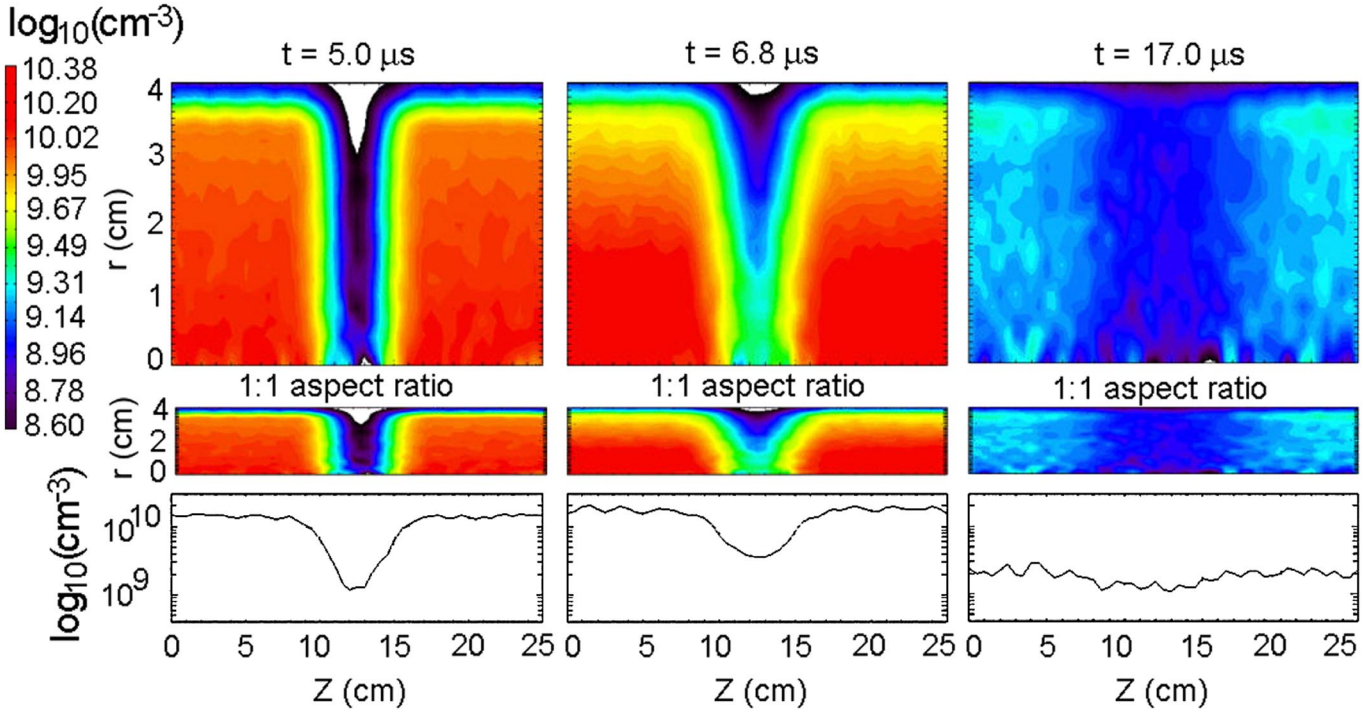

FIG. 12. (Color) n_p axial slices at $r = 0$ (bottom) and $\{r, z\}$ isocontours through $\theta = \pi$ (top) at $t = 5$ μs (left), $t = 6.8$ μs (center), and $t = 17$ μs (right). 1:1 aspect ratio $\{r, z\}$ plots are included (middle). All plots are on the same $\log_{10}$ scale.

about $\Delta t \sim +0.8$ μs after the peak density is achieved in the plasma-forming regions. Therefore, the axial regions initially vacant of plasma become filled with ~5× lower-density plasma within $\Delta t = +1$ μs after the time of global peak plasma density. The thermal energy is responsible for the maintenance of the plasma density above $n_p \sim 10^9$ cm^{-3} in the gap until $t = 17$ μs.

The comparison between the LSP code and the on-axis plasma density $n_p(t)$ measurements at the midplane of the ceramic segment is provided in Fig. 13. The measurements are similar in magnitude and duration to the simulation for the chosen initial conditions, $T_i = T_e = 20$ eV and $m_i^{\text{eff}} = 3 \times$ Ba. The initialized $v_r^i(t)$ and $J_r^i(t)$ profiles cause the plasma flow to coincide with the appropriate arrival time ($t \sim 6$ μs) and magnitude of the measured peak on-axis plasma density, as well as the accurate reproduction of the decay in the observed values of n_p at later times.

Presently, the comparison between simulation and experiment is qualitative because of the modest to high sensitivity of the results on the following five parameters. First, the initialized $v_r^i(t)$ and $J_r^i(t)$ are assumed, although based on realistic physical arguments. Second, as shown in Fig. 13, the on-axis electron temperature $T_e(t)$ drops monotonically in the experiment, possibly due to complex phenomena which are not included in the simulations. A constant $T_e = 20$ eV is chosen as the initial condition (and persists throughout the simulation), in order to match the average in the data. The inclusion of an electron energy sink is left for future simulations, since the relevant processes leading to a decreasing T_e in time are not well characterized experimentally. Third, the choice of effective ion mass m_i^{eff} is arbitrary. For the assumed T_e, ion mass choices other than $m_i^{\text{eff}} = 3 \times$ Ba alter the on-axis plasma density $n_p(t)$ (and its arrival time) because of the electron-driven acceleration of the ions into the central core. The use of lighter (heavier) ion species causes the arrival of on-axis peak n_p to occur earlier (later) in time, and its value to be less (greater) than the measured, since T_e determines the sheath strength and the acceleration increases (decreases) for smaller (larger) mass. Fourth, a colder (hotter) initial ion temperature T_i alters the on-axis $n_p(t)$ because the reduced (additional) thermal energies increase (decrease) the peak on-axis value and the amount of time the density persists in the source. Ion temperature measurements in the FEPS are not available at this time. Fifth, whether explosively formed ferroelectric plasmas are formed near thermal equilibrium requires further study. These insights indicate that the problem may admit multiple solutions or be far more complicated. Additional experimental determination of the aforementioned relevant quantities is desirable, as well as the inclusion in PIC simulation of neglected physics [such as the role of presently unknown neutral populations, the electron energy sink responsible for the measured decreasing $T_e(t)$, the possibility of recombination events, the actual processes involved in the breakdown at the surface of the dielectric material, and debris injected into the device from the surface explosions]. Even though there are many unknowns, the application of reasonable assumptions and the compelling comparison with measurements suggest that this model nevertheless provides insight into the ferroelectric plasma flow in such a device.

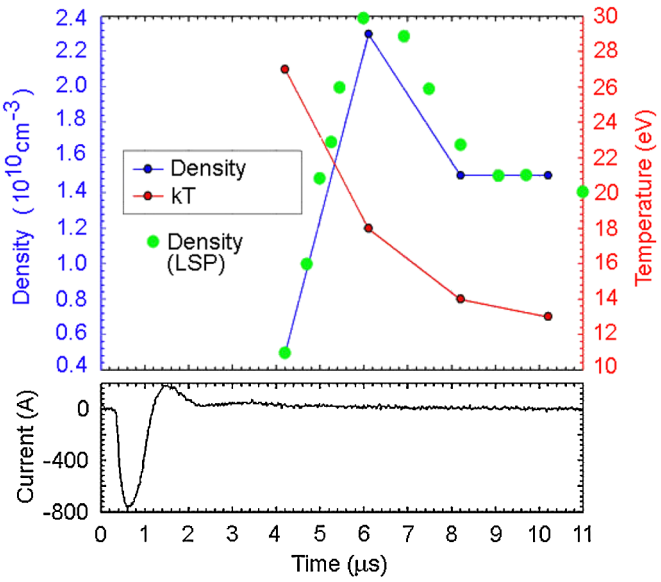

FIG. 13. (Color) On-axis $n_p(t)$ (top, blue) and $T_e(t)$ (top, red) measurements at the midplane of a ferroelectric ceramic segment, with discharge current shown (bottom). Comparison to $n_p(t)$ from simulation (top, green) is provided for the initial conditions $T_i = T_e = 20$ eV.

An issue of experimental importance resolved with simulation is whether nonuniform plasma creation in the azimuthal direction affects the plasma profiles. The desire to study such situations was stimulated by the observation that the azimuthal plasma formation conditions at the wall are not always uniform. During source operation, the emitted light from the plasma is not entirely θ-symmetric. Nonuniform emission may be expected from the ceramic rings if the geometry of the dielectric-microgap-mesh region is not uniform in the device (either due to construction or extended operation). Significant regions are found to be absent of light in some instances, prompting reassembly of the device to ensure taut (and uniform) front electrode conditions. Therefore, the question arises as to whether asymmetric plasma emission conditions severely modify the resulting plasma density profiles achieved in the plasma source.

Simulations indicate that asymmetric plasma creation conditions at the source walls nevertheless result in azimuthally symmetric profiles at the time of peak on-axis density. Four additional simulations are executed with one to four "holes" of nonemitting regions, each of which is $\Delta\theta = \pi/4$ and extends the entire axial distance.

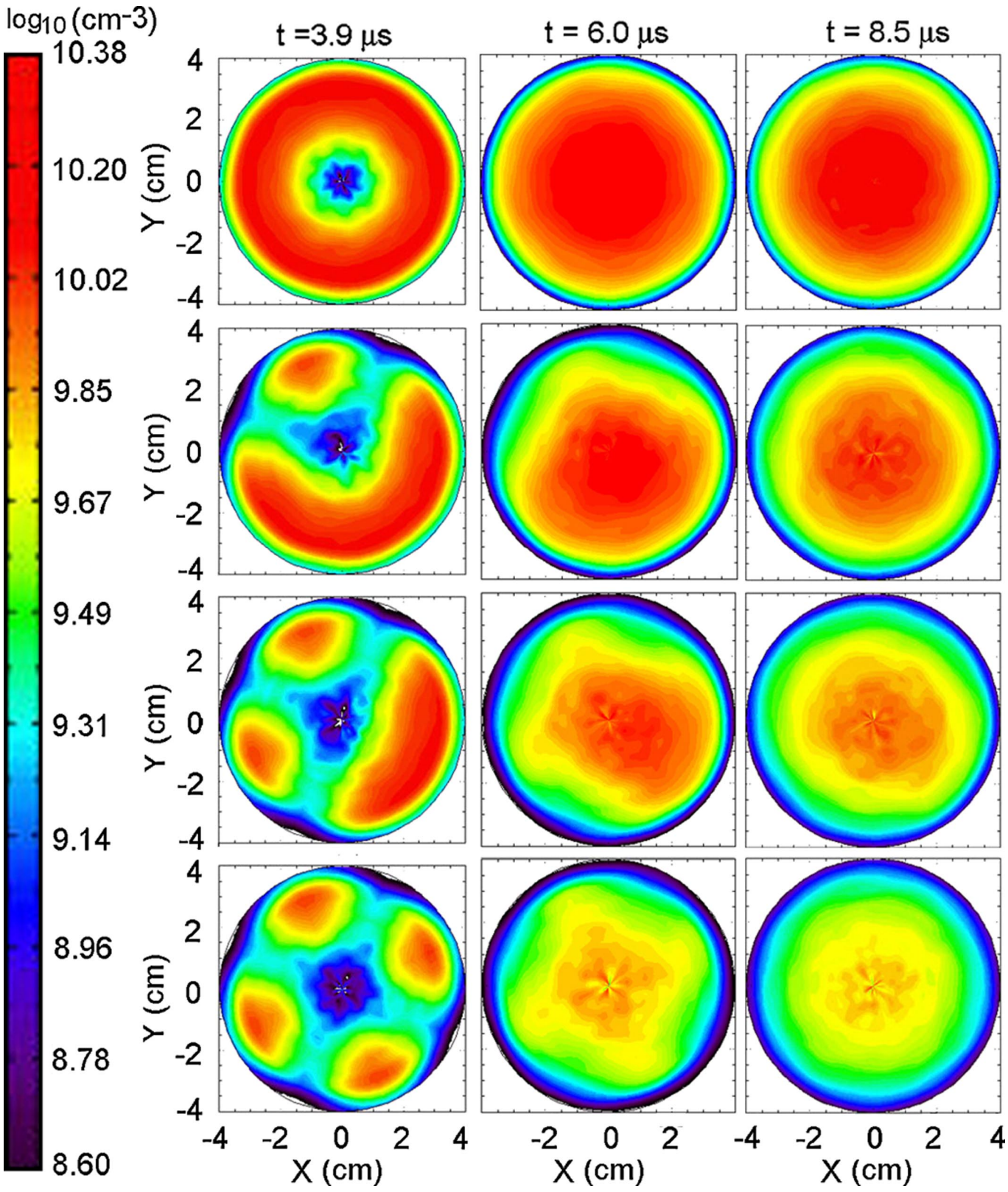

FIG. 14. (Color) $\{r, \theta\}$ isocontours of n_p through the midplane of a ceramic segment at $t = 3.9$ μs (left column), $t = 6$ μs (center column), and $t = 8.5$ μs (right column). Azimuthal holes of size $\Delta\theta = \pi/4$ approximate nonuniform emission effects: uniform plasma creation (first row), two holes (second row), three holes (third row), and four holes (fourth row). All plots are on the same $\log_{10}$ scale.

Therefore, the size of the simulated holes exaggerates the observations of the FEPS, but satisfactorily implies that nonuniform plasma creation conditions are manageable. Figure 14 illustrates three of the four azimuthally asymmetric simulations and provides the nominal case for reference (the missing case is only omitted for reasons of figure clarity). For early times ($t < 6$ μs), the plasma density n_p profiles resulting from nonuniform emission take on myriad shapes, and reflect the emission conditions at r_w. However, at the time of peak on-axis n_p ($t = 6$ μs), nonuniformities mostly disappear and symmetry is nearly established. By $t = 8.5$ μs, about $\Delta t \sim +2.5$ μs after realization of the peak n_p, the initial azimuthal asymmetry in plasma creation conditions is entirely absent. The role of thermal expansion is important in smoothing out nonuniform initial emission conditions. The values of n_p present at late times vary as a function of the amount of nonemitting area. This fact underlies the importance of using measurements to gauge the magnitude and temporal dependence of the achieved plasma density, in order to appropriately trigger the injection of the ion beam in compression experiments.

As mentioned earlier, the major difference between the FCAPS and FEPS is the method by which plasma fills the drift region. In the case of the former, plasma is injected towards the upstream end of the NDCX device. Besides the fact that the guide solenoid, electrostatic trap, and dipole required by the FCAPS complicate matters and use valuable axial estate, the directed movement of the cathodic-arc plasma is a concern if it allows electrons to penetrate beyond the intended plasma column and increase the emittance of the beam during transport. Therefore, in order to predict the amount of upstream penetration of the radially injected ferroelectric plasma without the additional components, additional simulations of the FEPS are carried out.

The difference between the present simulation, the result of which is shown in Fig. 15, and the previous cases is the removal of the axial periodic boundary conditions. Instead, extra vacuum chamber is modeled upstream of the ceramic rings (for $z < 0$) and a symmetry boundary condition is invoked at $z = +25$ cm. Since the plasma source injects with only $-v_r$ directed ion momentum, the axial motion of the plasma upstream (and into the gap regions) is solely due to thermal expansion. By the time of peak on-axis plasma density n_p ($t = 6$ μs), the plasma only penetrates $\Delta z \sim -4$ cm into the upstream region at levels $n_p > 10^8$ cm^{-3}. By $t = 11$ μs, the plasma has only traveled an additional $\Delta z = -4$ cm upstream (a total of $\Delta z \sim -8$ cm from its origin).

IV. PLASMA INJECTION INTO A STRONG MULTI-TESLA SOLENOID

The process of imposing an axial velocity tilt onto an intense ion beam as it traverses the acceleration gap of the induction module defocuses the otherwise radially converging trajectories of the ions in a time-dependent manner [5,10,15]. One proposed method for achieving simultaneous transverse and longitudinal compression to a coincident focal plane involves the use of a strong final-focus solenoid mounted near the end of the drift region. The magnetic field of the solenoid leads to radial focusing of the defocused charge bunch according to the Lorentz force, $-F_r = +q[(-v_\theta) \times (+B_z)] = -m_i(dv_r/dt)$. The solenoid reduces the effective transverse focal length involved because it defines the downstream location where the final radial focusing force is applied, thereby allowing the beam to transport to the solenoid at large radius instead of transversely converging through the entire plasma column. Therefore, less plasma can be used throughout the drift region, since the beam density n_b remains low until its radius r_b begins to significantly decrease within the final-focus solenoid. Also, intense charge bunches can be transversely compressed to sub-mm spot sizes, with smaller spots associated with stronger solenoids [8].

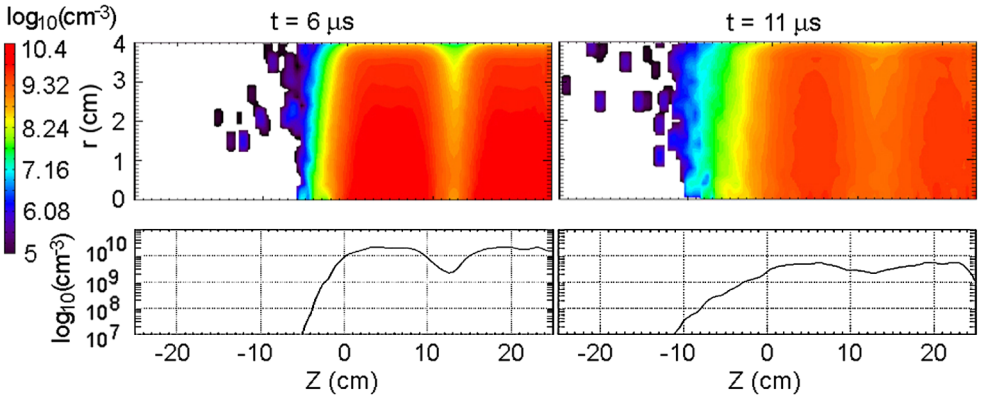

FIG. 15. (Color) n_p axial slices at $r = 0$ (bottom) and $\{r, z\}$ isocontours through $\theta = \pi$ (top) at $t = 6$ μs (left) and $t = 11$ μs (right). Because of space charge, the radially directed injection velocities, and the lack of magnetic guide field, electron populations do not axially move a significant distance. The plots are on $\log_{10}$ scales.

One challenge surrounding the use of a strong solenoid for beam compression experiments is the penetration of sufficiently dense plasma into the high-field region. Solenoids with magnitudes in the range $B_z \sim 30$–150 kG are under consideration, because of the desired beam energies, transverse focal lengths, and final spot sizes involved. As mentioned earlier, simulations suggest that plasma densities $n_p \sim 10^{12}$–10^{14} cm^{-3} or higher will be needed near the focal plane, depending on the strength of the focusing elements. One proposed method to fill such a solenoid with plasma is to longitudinally inject supersonic cathodic-arc plasma (as in Sec. II) into the high-field region [8,15].

The main difference between the simulations of Sec. II and those under discussion now is the considerable change in magnetic field strength from the guide solenoid ($B_z = 2$ kG) to the required final-focus strength ($B_z \sim 30$–150 kG). Because of the spacing between the filter coils of the cathodic-arc sources and final-focus solenoid, injected plasma must cross from low-field regions to a very high-field region. The large gradients in magnetic field strength parallel to $\hat{\mathbf{b}} = \mathbf{B}/B$ give rise to significant decelerating forces in the direction opposite the gradients. Both species become magnetized as they approach the final-focus solenoid. Recall the conservation of magnetic moment μ in the presence of an increasing magnetic field in the direction of $\hat{\mathbf{b}}$ leads to the magnetic mirror effect. Magnetic mirroring decelerates the injected plasma as it flows towards the high-field region, and is expected to be the determining factor for whether plasma can fill a strong solenoid. Therefore, its evaluation plays a significant role in the design considerations.

Generally, penetration into the high-field region only occurs for magnetized particles whose $v_\parallel/v_\perp$ ratio, where the directions are relative to $\mathbf{B}$, satisfies [25]

$$v_\parallel/v_\perp > \sqrt{\frac{B_{\max}}{B_{\min}} - 1}, \tag{2}$$

in the $B_{\min}$ region. Particles with larger $v_\parallel$ and smaller $v_\perp$ are expected to penetrate the high-field region, since particles with smaller initial $v_\perp$ experience smaller decelerating forces ($F_\parallel \sim -v_\perp^2$) as they approach regions of larger magnetic field. Magnetized particles with velocity ratios satisfying Eq. (2) fall into a "loss cone" in velocity space and experience deceleration, but are not completely reflected by the mirroring effect. Since the supersonically injected ions are more likely to have the necessary $v_\parallel/v_\perp$, they are expected to allow greater plasma penetration into the high-field region.

The 3D cathodic-arc plasma injection PIC simulations of Sec. II are revisited in order to study the evolution of the plasma flow in the presence of a final-focus solenoid. The goal is to study the coupling efficiency of the plasma flow from creation, through the curved filter coils, and into the final-focus solenoid. The coordinate system is the same as in Sec. II. However, the magnetic topology is significantly altered due to the relative magnetic field decrease in the filter coils to approximately $B_z = 0.45$ kG and increase within the final-focus solenoid to $B_z = 53$ kG. The offset $h = \pm 6$ cm and angle $\theta = \pm\pi/4$ are included as before, except two separation distance cases, $d = 8$ cm and $d = 16$ cm, are investigated.

Many parameters are retained from the original simulations in Sec. II, including the spatial resolution (0.5 cm) and the injection velocity in the $+\hat{y}$ direction for the Al^+ ions (1.44 cm μs^{-1}). However, the peak ion current density is increased to $J_p^i \sim 2$ A cm^{-2} (from 0.04 A cm^{-2}), corresponding to a peak plasma density of $n_p \sim 10^{13}$ cm^{-3} near the sources. Maxwellian distributions with temperatures $T_i = 3$ eV and $T_e = 10$ eV are imposed on the ion and electron populations, respectively, corresponding to an injected ion Mach number of approximately 1.7. Scattering effects between charged particles are included by using Spitzer rates [3]. The simulation is executed to $t = 25$ μs with a time step satisfying the constraints $\omega_{pe}^{\text{peak}}\Delta t < 0.2$ and $\omega_{ce}^{\text{peak}}\Delta t < 1$ (about 2.5×10^7 total steps). During steady-state plasma flow ($t \sim 20$ μs), more than 5×10^5 particles are explicitly pushed on the simulation grid at each time step.

Simulation results for the $d = 8$ cm and $d = 16$ cm cases using a final-focus solenoid of strength $B_z = 53$ kG are presented in Fig. 16 in the form of $\{y, z\}$ isocontours of plasma density during steady state flow through the $x = 0$ axis. The n_p profiles are directly comparable to the top right frame in Fig. 5, except for the relative increase in initial J_p by the factor of 50. Both species become magnetized in the region between the three solenoids, and largely follow field lines while executing guiding-center drift orbits. Significant levels of magnetic mirroring occur in both cases. The case with the shorter d couples plasma into the final-focus solenoid, but the n_p is lower at the $z = 0$ axis than off axis, which is not desirable for beam compression experiments. Conversely, the $d = 16$ case illustrates plasma filling the solenoid with peak density located on axis, as observed more clearly in Fig. 17. Both cases only partially fill ($r_p^{\text{fill}} < r_{\text{sol}}$) the strong solenoid.

The $\{x, z\}$ isocontours of plasma density during steady-state flow at various y locations demonstrate that the $d = 16$ cm case fills the $B_z = 53$ kG solenoid with more uniformity in the $\{x, z\}$ planes (the θ direction) than the $d = 8$ cm case. Essentially, the increased separation d gives the plasma more time and space to execute its complex 3D plasma motion. The $d = 8$ cm case does not undergo enough electron guiding-center drift in the $\pm\hat{x}$ direction in order to symmetrically fill the solenoid with plasma, as manifest in the profiles shown in Fig. 17. Therefore, the larger d case is better for beam compression experiments, since the n_p is uniform and centered on the beam's axis of

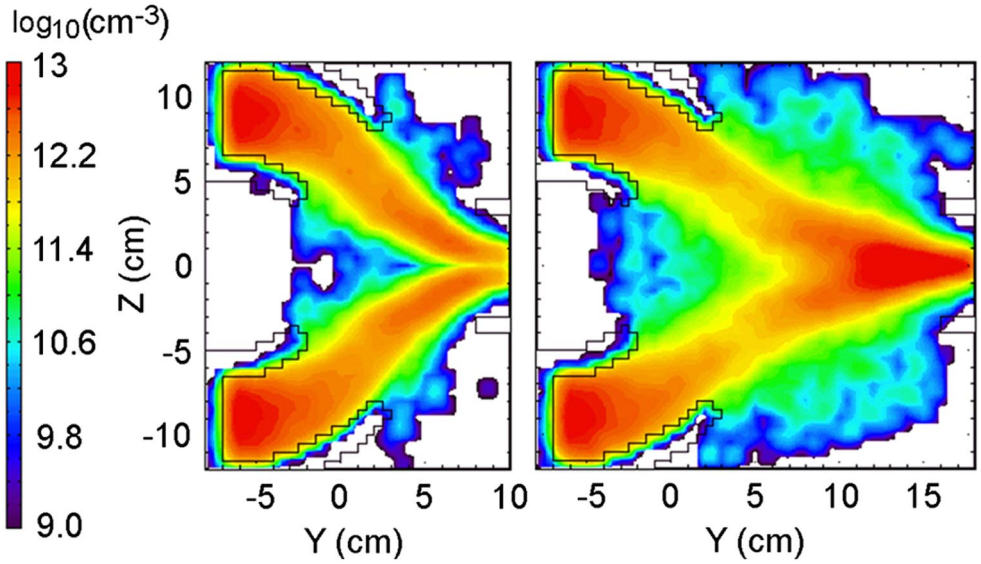

FIG. 16. (Color) $\{y, z\}$ isocontours of n_p ($\log_{10}$ scale) through the $x = 0$ axis for the case of cathodic-arc plasma injection into a $B_z = 53$ kG final-focus solenoid, with a separation distance $d = 8$ cm (left) and $d = 16$ cm (right). The $d = 16$ cm case is similar to the configuration planned for future experiments.

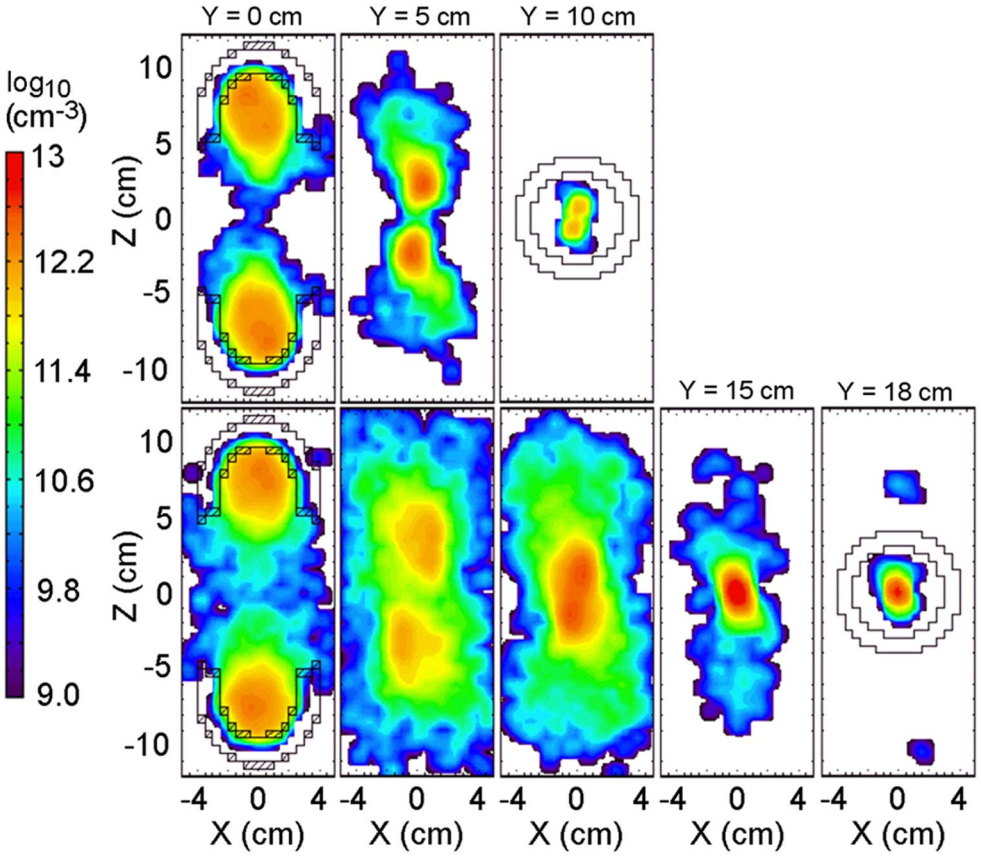

FIG. 17. (Color) $\{x, z\}$ isocontours of n_p ($\log_{10}$ scale) through various y locations for the case of cathodic-arc plasma injection into a $B_z = 53$ kG final-focus solenoid, with a separation distance $d = 8$ cm (top) and $d = 16$ cm (bottom).

propagation ($z = 0$ in the $-\hat{y}$ direction). Apparently, the separation distance makes a significant difference to the dynamics of the plasma flow, since it (and other parameters) affects the local magnetic topology experienced by the injected plasma.

Additional 2D $\{r, z\}$ LSP simulations of plasma flow into a $B_z = 40$ kG final-focus solenoid are performed in order to further investigate the feasibility of plasma filling using a cathodic-arc plasma source. The main reasons the simulations are carried out in reduced-dimensionality cylindrical geometry are to decrease the computational requirements and increase the spatial resolution of the nonphysical particle-in-cell grid, since increased resolution of the density and velocity profiles is desired in the fringe-field and $r = 0$ regions. In addition, parameter scans can more efficiently be carried out, with increased resolution, in the 2D simulations. Implicit methods for pushing electron particles in LSP [3,38–40] can be used in order to under-resolve either the electron cyclotron (ω_{ce}) or plasma frequency (ω_{pe}), but not both at the same time. Because of the large plasma densities under consideration ($n_p \sim 10^{12}$–10^{14} cm^{-3} or higher), the employment of implicit particle-pushing methods is not cost effective (and not used in any of the simulations presented here) because ω_{ce} is within an order of magnitude of ω_{pe} (both are between 5–8 $\times 10^{11}$ rad s^{-1} for $B_z \sim 40$ kG and $n_p \sim 10^{14}$ cm^{-3}).

The $\{r, z\}$ simulation grid extends from $r = 0$ to $r = 4$ cm and $z = -10$ cm to $z = +20$ cm, with a spatial resolution of $\Delta r = 0.05$ cm and $\Delta z = 0.2$ cm. A 10 cm-long, $B_z = 40$ kG solenoid with inner radius $r^{\mathrm{sol}} = 4$ cm is positioned between $z = -5$ cm and $z = +5$ cm. The solenoidal magnetic field in cylindrical geometry is calculated in LSP for off-axis values according to a sixth-order power series expansion in the radial coordinate of an ideal finite-length solenoid [41]. Cathodic-arc plasma injection occurs in the upstream direction from the downstream end, at the injection plane $z = +20$ cm in the low-field region. A conducting boundary at $r_w = 3.8$ cm and open axial boundaries are modeled. Since the intended simultaneous focal plane of the intense beam may lie within (or just beyond) the solenoid, the plasma density profiles within (and downstream) of the solenoid are important to evaluate.

The magnetic field topology in the simulation is shown in Fig. 18. The beam would travel in the $+\hat{z}$ direction in this coordinate system, centered on the $r = 0$ axis (the beam is not included in this simulation). The filter coils and sources of the cathodic-arc plasma source are not modeled due to the reduction in dimensionality. Therefore, the assumption is made to continually inject a constant $\{r, \theta\}$ profile of the approximate maximum experimental plasma density $n_p \sim 10^{12}$ cm^{-3} (over $\theta = 2\pi$) at the injection plane in the low-field region, from $r = 0$ to $r = 3.8$ cm, until a steady-state solution is reached. The steady-state density solutions include the contribution to total density on the downstream end of the solenoid from that plasma which is reflected away from the high-field region. Maxwellian distributions with temperatures $T_i = 1$ eV and $T_e = 5$ eV are imposed on the injected ion and electron populations, respectively. The plasma beta is very small in this simulation due to the large magnetic pressure associated with the $B_z = 40$ kG field. Scattering effects between charged particles are included by using Spitzer rates [3]. The simplification of the magnetic field topology, due to the reduction in dimensionality from 3D to 2D, is an adequate approximation because the field approximately 5–10 cm downstream from the final-focus solenoid is dominated by the final-focus solenoid fringe contribution, and not by those fringe fields from the guide solenoids. The simplification of the injection model is also reasonable because the plasma densities become roughly uniform in

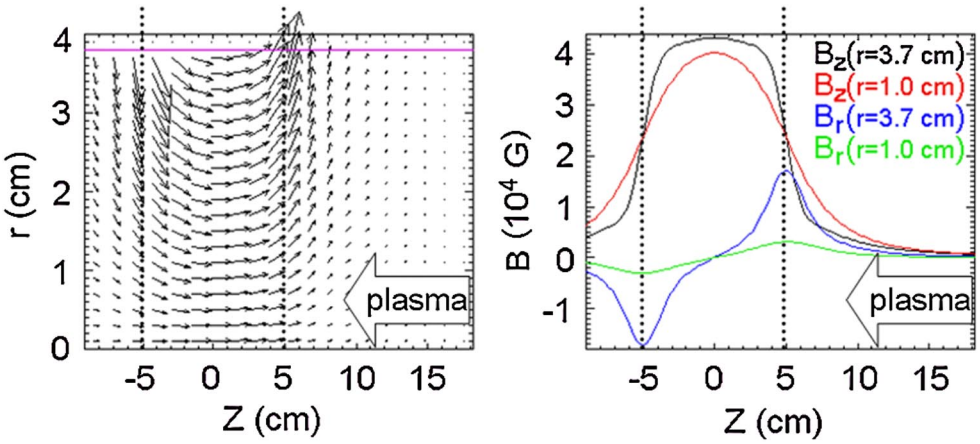

FIG. 18. (Color) Magnetic field vector plot (left) and axial slices of the $B_r(z)$ and $B_z(z)$ magnetic field components at $r = 1$ and $r = 3.7$ cm (right). Constant $n_p \sim 10^{12}$ cm^{-3} with $v_z^i = -1.44$ cm/μs is injected in the upstream ($-\hat{z}$) direction, towards the $B_z = 40$ kG solenoid, as illustrated with arrows. The beam would travel in the $+\hat{z}$ direction in this coordinate system. Dotted lines indicate the position of the solenoid.

$\{r, \theta\}$ between ~5–10 cm downstream of the final-focus solenoid (refer to the bottom frame of Fig. 17), and so justify the approximation of azimuthal uniformity imposed in 2D $\{r, \theta\}$ simulations when injecting plasma from a similar axial location (compare to Fig. 18).

In order to determine the dependence on supersonic cathodic-arc ion injection velocity for filling the strong solenoid with plasma, four simulations are conducted using the initial velocities $v_z^i = -1.5$ cm μs^{-1}, -3 cm μs^{-1}, -6 cm μs^{-1}, and -12 cm μs^{-1} (corresponding to initial ion Mach numbers of 2.7, 5.5, 11, and 22, respectively). In order to maintain the same initial constant $n_p \sim 10^{12}$ cm^{-3}, the current densities are $J_p^i = 0.3$ A cm^{-2}, 0.6 A cm^{-2}, 1.2 A cm^{-2}, and 2.4 A cm^{-2}, respectively. The simulations are executed to $t = 30$ μs with a time step satisfying the constraints of $\omega_{pe}^{\text{peak}} \Delta t < 0.68$ and $\omega_{ce}^{\text{peak}} \Delta t < 0.85$ (about 2.5×10^7 total steps). During steady-state plasma flow, more than 1.6×10^6 particles are explicitly pushed on the simulation grid at each step.

Figure 19 illustrates 2D $\{r, z\}$ isocontours of plasma density n_p during steady-state plasma flow for the four injection velocity cases. The simulations indicate that the $B_z = 40$ kG solenoid becomes partially filled by the high-density FCAPS, beginning at different times (depending on the injected v_z^i, but is $t \sim 12$ μs for the slowest). As before, an electron sheath accelerates the ion fronts early in time. Ion magnetization occurs later, so they are able to penetrate farther (in the $-\hat{z}$ direction) before becoming tied to the field lines, and facilitate the penetration of the electrons into the same regions due to space charge. Magnetized plasma flows along field lines and, in some locations, the n_p is compressed by more than an order of magnitude, which helps to achieve density requirements needed for beam compression experiments. The peak density $n_p \sim 10^{14}$ cm^{-3} is found near the "bottleneck" region, located near the downstream end of the final-focus solenoid, where a majority of the plasma is reflected by the strong magnetic field. It is possible that the majority of the plasma might not be reflected if the magnetic field in the sources is increased, provided that the filter coil currents are not an experimental limitation. The fields in the sources are known to affect the plasma jet properties, such as the ion kinetic energy and charge state. Also, different separation distances, angles, and height offsets might help improve the coupling efficiency of the plasma into the high-field region.

Because of the magnetic mirroring effect, plasma particles streaming into the solenoid generally decelerate due to the $\mathbf{F}_\parallel = -\mu \nabla B$ force and many are reflected away from the high-field region, as shown in Fig. 20. Much of the initial injected energy is transferred from parallel into perpendicular energy. The effect dominates the plasma dynamics in this particular scenario because of the final-focus solenoid magnetic field involved, and reduces the amount of plasma able to fill the solenoid. As plasma reaches the edge of the solenoid at $z = +5$ cm, where B_r reaches a maximum, a majority of the plasma is reflected into the $+\hat{z}$ direction, since only particles with high enough $v_\parallel / v_\perp$ ratios are able to penetrate the high-field region. Most of those able to do so are supersonic ions, and

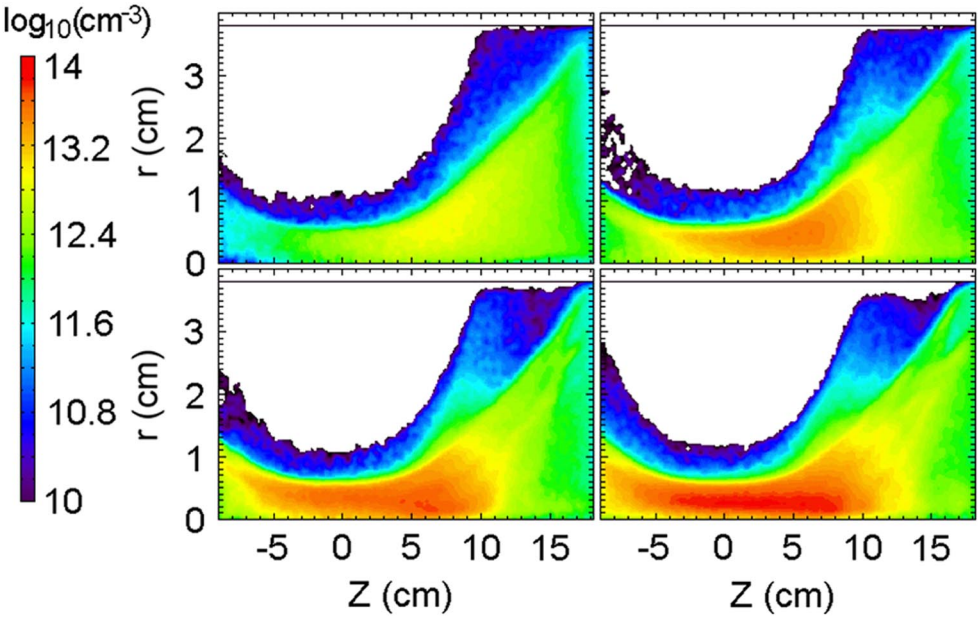

FIG. 19. (Color) n_p isocontours at $t = 30$ μs during steady-state plasma flow into a $B_z = 40$ kG solenoid, for initial ion injection velocities $v_z^i = -1.5$ cm μs^{-1} (top left), -3 cm μs^{-1} (top right), -6 cm μs^{-1} (bottom left), and -12 cm μs^{-1} (bottom right). All plots are on the same $\log_{10}$ scale.

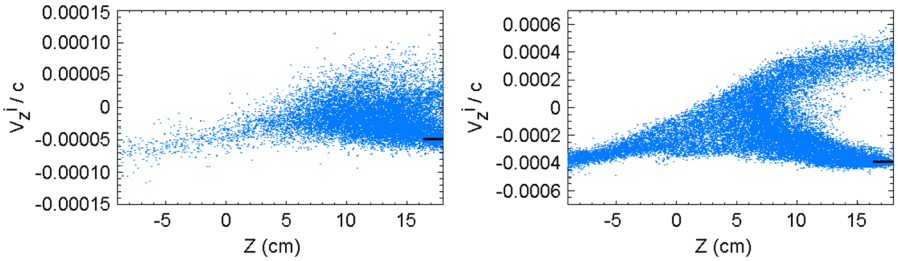

FIG. 20. (Color) $\{z, v_z\}$ plasma ion phase space plots for the cases of initial $v_z^i = -1.5$ cm μs^{-1} (left) and $v_z^i = -12$ cm μs^{-1} (right). Counterpropagating ion streams (due to mirroring) are evident for $z > 2$ cm. Horizontal black bars demarcate the injected initial v_z^i on both plots.

electrons largely follow the ion movement into the solenoid via the electric field from the ambipolar potential; as the v_z^i increases, the amount of plasma density able to penetrate the solenoid does as well. In each case, the plasma fills the solenoid to an approximate radius $r_p^{\text{fill}} \sim 0.6$ cm. The bottleneck buildup of n_p near the edge of the final-focus solenoid, where the average plasma flow velocity is a minimum, is simultaneously due to compression along field lines as well as contributions from reflected plasma. Counterpropagating ion streams are found on the downstream end of the final-focus solenoid, as illustrated in Fig. 20.

V. NEUTRALIZATION EFFECTS ON SIMULTANEOUS FOCUS

At the present time, the compression of intense ion beams in the laboratory has been separately demonstrated in the transverse and longitudinal directions. However, simultaneous focusing to a common focal plane is desired in order to maximize the intensity on the target for a given amount of initial beam charge. The goal for upcoming experiments is to demonstrate the feasibility and study the physical limitations of simultaneous transverse and longitudinal compression of an intense charge bunch [8,9,42].

In this section, the focus of the paper shifts from the simulation of the plasma sources towards assessing the effects of neutralization on beam compression experiments. Specifically, this section provides simulations that directly study the simultaneous transverse and longitudinal focusing of an intense ion beam in the presence of plasma sources, but by making various assumptions about the background plasmas. First, the overfocusing technique for simultaneous transverse and longitudinal beam compression will be introduced, and simultaneous focusing results in the perfectly neutralized limit will be compared to the opposite limit, where no neutralizing plasma is available. Second, partial neutralization effects on beam compression will be examined under a variety of plasma conditions, including the dynamic FEPS plasma from Sec. III and various background plasmas initialized with spatially uniform densities and temperatures.

A. The overfocusing technique

As mentioned in Sec. IV, the process of imposing an axial velocity tilt inadvertently contributes a net divergence, in a time-dependent manner, to the otherwise radially converging trajectories of the beam ions. The time-dependent nature of the induction module voltage waveform, combined with the transit time of the ion particles across the acceleration gap, imply an imbalance of $E_r(r, z, t)$ experienced by each particle on the upstream and downstream ends of gap, and provides radial defocusing to the entire charge bunch.

Various separate methods exist to compensate for the defocusing effect in the acceleration gap in order to achieve focused beam radii of a few mm or less at the simultaneous focal plane. The simplest method for recovering the proper transverse beam ion trajectories would be to give the charge bunch too large a convergent angle as it exits the magnetic transport section and enters the acceleration gap of the induction module (refer to Fig. 2). An optimized angle can be found for which the excess amount of focusing is balanced by the defocusing effect, causing the beam to transversely focus to its originally intended location [15]. However, since the excess divergence given to the beam is time dependent, the so-called ''overfocusing'' technique can only offset the defocusing effect in an average way. In other words, there will still be a time-dependent range of convergence angles about the central portion of the compressing charge bunch, with larger discrepancies found farther from the center, which give rise to transverse focusing aberration.

To illustrate the technique, a 2D $\{r, z\}$ PIC simulation of regular transverse focusing with an axial velocity tilt is compared to an overfocused case. An $E_b = 300$ keV K^+ beam with an initial radius $r_b = 2$ cm and current $I_0 = 18$ mA is initialized with a Maxwellian $T_\parallel = T_\perp = 0.2$ eV temperature. It is given a convergence angle of approximately $\Delta\theta_r = -15.4$ mrad at the injection plane $z = -30$ cm, just downstream of the magnetic transport section and upstream of the 3 cm-long acceleration gap (which is located from $z = -22$ cm to $z = -19$ cm in this coordinate system). These beam parameters are in good agreement with those measured or inferred in NDCX ex-

periments. The coordinate system extends from $z = -30$ cm to $z = +110$ cm, the plasma nominally begins near $z \sim 0$, and the conducting outer wall of the beam line has a radius of $r_w = 3.8$ cm.

The application of a radial convergence angle onto the beam by the final transport magnet upstream of the acceleration gap causes the $-v_r$ of the beam particles to vary radially as $-v_r(r) = -v_z^0(r/r_b)(r_b/L_r)$ for $r = 0$ to $r = r_b$, where L_r is the radial focal length (note that $\Delta\theta_r \equiv -r_b/L_r$). Ignoring the defocusing effect, one would normally desire $L_r \sim L_d$ (for an L_r defined near the gap) for simultaneous transverse and longitudinal focusing, where L_d is the longitudinal focal length determined by the applied axial velocity tilt. The initial pulse length of the beam is $t_p = 700$ ns and the experimental induction module voltage waveform imposes an approximate 10% axial velocity tilt, defined as $f \equiv \Delta v_z/v_0$, where v_0 is the initial beam velocity. In this case, the background plasma from $z = +5$ cm to $z = +110$ cm (the approximate range in experiments) is sufficiently dense and cold to ensure good neutralization throughout the entire drift length. Therefore, the field equations are not advanced so that the simulations in Sec. VA represent the idealized ''completely neutralized'' cases of purely ballistic ion beam focusing.

The longitudinal focal plane is located at $z = +95$ cm (the total drift length is $L_d \sim 117$ cm) at $t = 1320$ ns and the beam achieves an axial compression ratio of 67 (defined as $I_b^{\max}/I_0$) with a full-width, half-maximum pulse length $t_{\text{fwhm}} = 1.7$ ns, in good agreement with some of the most recent measurements (note that the voltage waveform only applies the compressing velocity tilt to a fraction of the initial pulse length). In the regular transverse focusing case, r_b^{foc} at the focal plane is also ~ 2 cm due to the defocusing effect. The impact of the defocusing effect on current density compression, and therefore energy deposition for warm dense matter and heavy ion fusion applications, is striking because of the inverse dependence on the square of the radius [$J_z \sim r_b(t)^{-2}$].

The regular transverse focusing case is repeated, except with the simple change from $\Delta\theta_r = -15.4$ mrad to -32.3 mrad at $z = -30$ cm, and the difference in beam density n_b evolution in such an overfocused case is demonstrated in Fig. 21. In the regular focusing case, the beam density $n_b^{\text{foc}}(r) \sim 1.4 \times 10^9$ cm^{-3} is approximately constant at the focal plane as a function of radius with a sharp edge near $r \sim 2$ cm, whereas the overfocused beam reaches a peak on-axis density $n_b^{\text{foc}} \sim 2.3 \times 10^{11}$ cm^{-3} with much smaller r_b^{foc}. Figure 22 shows the striking difference in transverse compression. The $\Delta\theta_r = -15.4$ mrad beam at the focal plane has an rms radius of ~ 1.4 cm (not indicative of the nearly constant profile), whereas the overfocused beam achieves an rms radius of $r_b^{\text{foc}} \sim 0.125$ cm (similar to the $1/e$ radius). The longitudinal compression in both cases is the same, as shown in the blue curve of Fig. 22, but the r_b^{foc} difference accounts for a factor of 250 in J_z.

The cumulative energy deposition profiles $E_{\text{dep}}(r)$ (defined as the calculated energy densities from the particle velocities and densities passing through the specified plane) over the entire duration of the pulse for both cases are also presented in Fig. 22. The beam with the larger initial $\Delta\theta_r$ achieves twice the peak on-axis E_{dep} compared to the nominal case. However, the proportion of the deposition residing within the main compressed pulse is vastly different between the two, as evident in Fig. 23. The prepulses and postpulses (the first ~ 222 ns and last ~ 475 ns, respectively) in the nominal case contain the overwhelming majority of the time-integrated E_{dep} at the focal plane, and the significant relative contrast between them and the main pulse is undesirable for applications involving targets. Conversely, upon comparison of Figs. 22 and 23, approximately 80% of the peak on-axis E_{dep} in the overfocused case resides within the main 3 ns of compressed pulse. The preheat impinging the target is 20%–30% of that delivered by the main pulse, with 50% of the prepulse deposition within the final 4 ns prior to the main

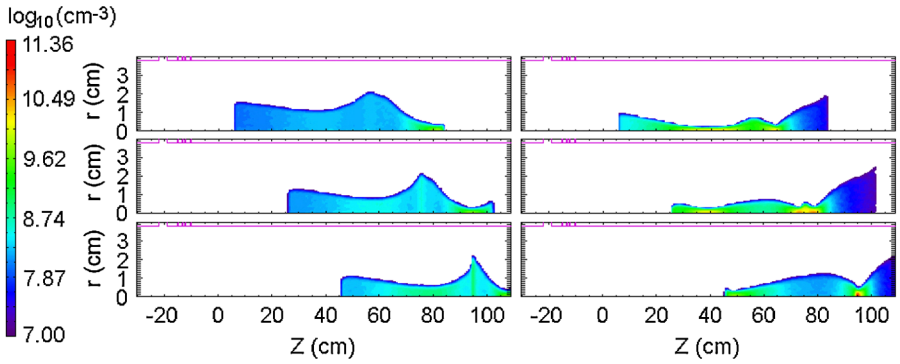

FIG. 21. (Color) $\{r, z\}$ isocontour plots of beam density n_b at $t = 1000$ ns (top row), $t = 1160$ ns (middle row), and near focus at $t = 1320$ ns (bottom row) for the regular transverse focusing $\Delta\theta_r = -15.4$ mrad case (left column) and the overfocused $\Delta\theta_r = -32.3$ mrad case (right column). All plots are on the same $\log_{10}$ scale.

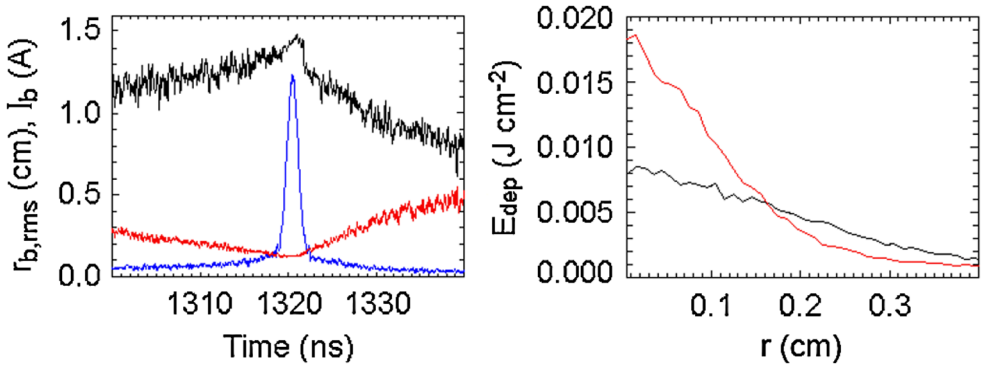

FIG. 22. (Color) Time history plots (left) of $I_b(t)$ (blue) and rms $r_b(t)$ for $\Delta\theta_r = -15.4$ mrad (black) and -32.3 mrad (red) and cumulative energy deposition profiles $E_{\mathrm{dep}}(r)$ (right, same color code) over the entire pulse length t_p at the focal plane. Both cases achieve the same longitudinal compression (blue), and the peak $I_b = 1.21$ A corresponds to $I_b^{\max}/I_0 = 67$.

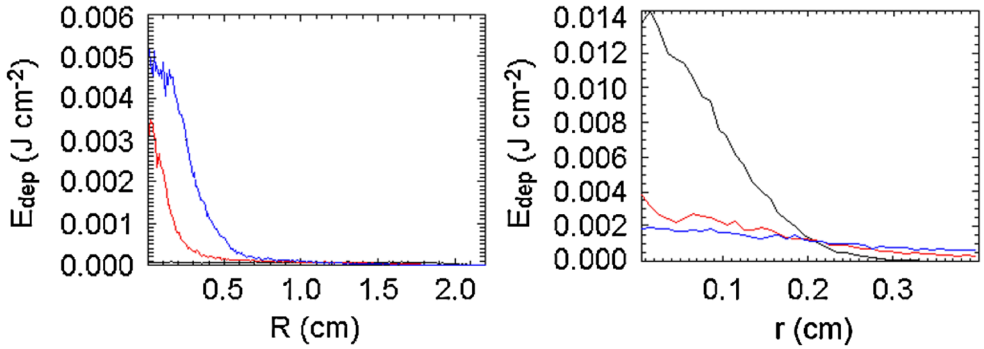

FIG. 23. (Color) Cumulative $E_{\mathrm{dep}}(r)$ profiles for the ~222 ns of prepulse before $t = 1319$ ns (red), 3 ns of main pulse from $t = 1319$–1322 ns (black), and ~475 ns of postpulse after $t = 1322$ ns (blue) at the focal plane for the $\Delta\theta_r = -15.4$ mrad (left) and -32.3 mrad (right) cases. Note the difference in scales, and the main pulse $E_{\mathrm{dep}}(r)$ for the case on the left is constant at $\sim 6 \times 10^{-5}$ J cm^{-2} to $r = 2$ cm.

pulse. The case presented here is intended to be illustrative of the mentioned effects and methods, and does not necessarily represent the optimal devisable configuration.

The overfocusing technique is the simplest time-independent way to mitigate the defocusing effect in an averaged way. The natural extension of this technique implies the use of time-dependent magnetic focusing in the transport section to separately alter the $\Delta\theta_r$ of different portions of the beam pulse and thereby negate the time-dependent divergence added to the beam by the gap. Time-dependent magnetic focusing enjoys active research as a promising method for relieving the disruption to the transverse beam dynamics during the application of velocity tilts. However, the technology to achieve the necessary $d\mathbf{B}(t)/dt$ is not currently available.

B. Partial neutralization effects

The provision that the background plasma density be much greater than the beam density throughout the drift length ensures high levels of beam neutralization during simultaneous compression. In order to quantify the effects of partial neutralization compared to cases of complete neutralization, a series of PIC simulations are computed in a variety of plasma conditions [15]. Incomplete neutralization effects are expected to contribute to decreased levels of compression in both directions for cases involving total J_z compression factors greater than 10^4. The primary concern for most intense beam applications is the degradation of the minimum beam radius at focus.

The simultaneous focusing simulations involving regular and overfocused initial $\Delta\theta_r$ are revisited, except the background plasma is removed. In other words, the self-fields of the beam self-consistently evolve with the dynamically compressing beam, whose particle velocity distributions change in time due to the self-fields and boundary conditions. The simultaneous compression results are plotted in Fig. 24 as time history plots of rms $r_b(t)$ and $I_b(t)/I_0$ at the focal plane. Without plasma present, the radial self-electric fields are not neutralized and resist the initial $\Delta\theta_r$, leading to radial divergence before reaching $z \sim +30$ cm. The rms $r_b(t)$ values at the intended longitudinal focal plane are greater than the initial $r_b = 2$ cm

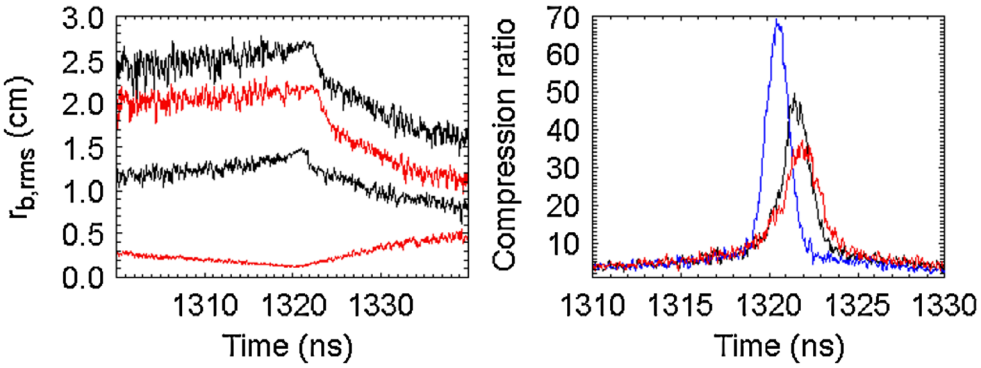

FIG. 24. (Color) Time history plots of rms $r_b(t)$ (left, top profiles) and compression ratio $I_b(t)/I_0$ (right) at the intended focal plane ($z = +95$ cm) without background plasma for $\Delta\theta_r = -15.4$ mrad (black) and -32.3 mrad (red). For reference, the completely neutralized color-coded cases from Fig. 22 for the rms $r_b(t)$ (left, bottom profiles) and compression ratio $I_b(t)/I_0$ (right, blue) are provided.

for both cases, although the rms quantities do not reflect the nearly constant radial density profiles of $r_b \sim 3.5$ cm with $n_b \sim 3.5 \times 10^8$ cm^{-3} ($E_{\rm dep} \sim 1.5 \times 10^{-5}$ J cm^{-2}) for the -15.4 mrad case and $r_b \sim 2.8$ cm with $n_b \sim 5.5 \times 10^8$ cm^{-3} ($E_{\rm dep} \sim 2.3 \times 10^{-5}$ J cm^{-2}) for the -32.3 mrad case. The self-field effects alter the longitudinal dynamics as well, since the current compression also suffers; although, the $I_b^{\rm max}/I_0 = 67$ is recovered farther downstream from the intended focal plane ($\Delta z = +3$ cm and $+5$ cm for the -15.4 mrad and -32.2 mrad cases, respectively) because the large r_b ensures the self-potential is too small to significantly alter the axial trajectories of the $\sim$300 keV K^+ ions. Such a result also highlights the coupling of the transverse and longitudinal dynamics, as well as the possible separation of focal planes.

To ascertain the neutralization level provided by the ferroelectric plasma source (Sec. III) for NDCX-relevant parameters, the overfocused $\Delta\theta_r$ simulation is executed again, except background plasma is modeled by the dynamic simulation of radially injected ferroelectric plasma. Five 15 cm segments of the FEPS (with four 5 cm transverse ports) are modeled between $z = +7$ cm and $z = +102$ cm, in order to align the focal plane within the last region of high-density plasma. The ferroelectric source plasma flow simulation uses the same input parameters mentioned in Sec. III. The timing of the beam relative to the ferroelectric plasma injection is $\Delta t = +5$ μs, so that the simultaneously compressing charge bunch arrives at the focal plane approximately at the time of peak on-axis plasma density (refer to Fig. 13). The results are presented in Fig. 25 and show that the beam density does not reach the same peak value at the focal plane (as shown in the bottom right frame of Fig. 21) in the presence of the dynamic ferroelectric plasma, due to radial focal spot degradation (longitudinal compression is unaffected).

The peak on-axis beam density of the completely neutralized overfocused beam from Sec. VA is $n_b^{\rm foc} \sim 2.3 \times 10^{11}$ cm^{-3} with rms $r_b^{\rm foc} \sim 0.125$ cm. Since the peak on-axis plasma density achievable by the FEPS is $n_p^{\rm foc} \sim 2.5 \times 10^{10}$ cm^{-3} around $t = 6$ μs, the expected peak n_b would exceed the supplied peak n_p near the focal plane. Plasma electrons respond to the overabundance of ions and the self-fields of the beam by executing orbits that minimize the charge perturbation. However, the cumulative effect of the partial neutralization along the drift length is manifest in terms of a larger $r_b^{\rm foc}$ and smaller peak $E_{\rm dep}$ at the focal plane, as plotted in Fig. 26. The partial neutralization effects of the FEPS on the beam compression doubles the minimum rms radius from $r_b^{\rm foc} = 0.125$ cm to 0.25 cm, implying reasonable levels of neutralization are provided (the unneutralized case yields $r_b^{\rm foc} = 2.2$ cm). The peak on-axis cumulative energy deposition from the main pulse decreases from $E_{\rm dep}^{\rm foc} \sim 0.014$ J cm^{-2} to $\sim$0.003 J cm^{-2} with $r_b^{\rm foc} \sim 0.35$ cm ($1/e$), whereas the peak on-axis beam density is $n_b^{\rm foc} \sim 3 \times 10^{10}$ cm^{-3}, almost an order of magnitude lower than the completely neutralized

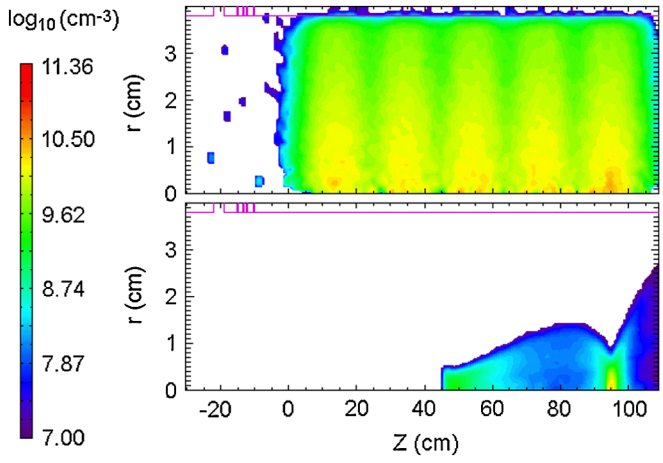

FIG. 25. (Color) $\{r, z\}$ isocontours of ferroelectric plasma density n_p (top) and beam density n_b (bottom) near the simultaneous focal plane at $t = 6320$ ns. Both plots are on the same $\log_{10}$ scale.

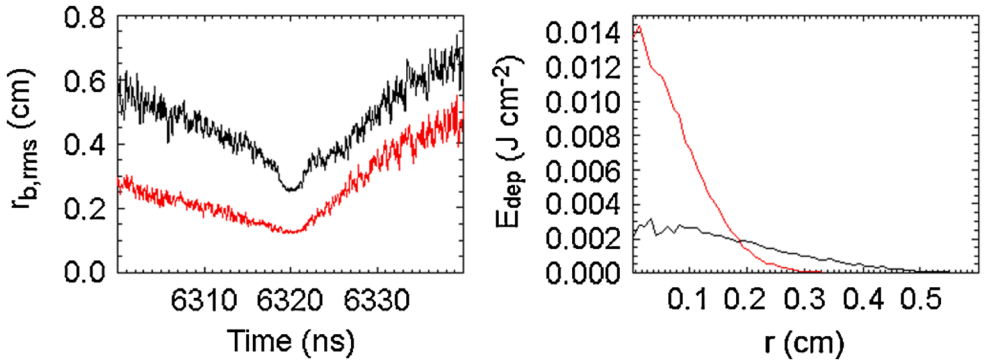

FIG. 26. (Color) Time history plots of rms $r_b(t)$ (left) and radial profiles of cumulative $E_{\mathrm{dep}}(r)$ from the main pulse from $t =$ 6319–6322 ns (right) at the focal plane using an initial $\Delta\theta_r = -32.3$ mrad, and the dynamic ferroelectric plasma simulation for neutralization (black). For reference, the completely neutralized case (red) results from Figs. 22 and 23 are provided, with the $\Delta t =$ $+5$ μs temporal shift included.

case. Clearly, the supplied plasma density $n_p \sim 2.5 \times 10^{10}$ cm^{-3} is too low and plasma temperature $T_p \sim 25$ eV is too high to provide the neutralization required to asymptote to the completely neutralized case.

A sequence of PIC simulations is calculated to quantify the partial neutralization effects from variations in initial plasma density. The overfocused simulation from Sec. VA is repeated in the presence of an initialized spatially uniform plasma whose densities decrease from $n_p = 10^{12}$ cm^{-3} to $n_p = 10^7$ cm^{-3} (in steps of 10^{-1} cm^{-3}) without initial T_p, located from $z = +5$ cm to $z = +110$ cm. A cold electron emission model in LSP emits those particles from the conducting wall at $r_w = 3.8$ cm, provides a copious supply of electrons (by replacing those lost to the boundaries), and alters the sheath physics by facilitating a more quiescent plasma response to the injected beam. The extra electron population is important to consider in the lowest n_p cases, since the initial beam density $n_b > 10^8$ cm^{-3} as the beam enters the plasma and the emission electrons participate in the interaction process between the beam and plasma for cases when $n_p \gg n_b$ is not adequately satisfied.

The simultaneous compression results from the cases of various initialized cold plasmas are plotted in Fig. 27. The cases involving $n_p = 10^{10}$–10^{12} cm^{-3} recover the completely neutralized results (minimum rms r_b^{foc} and peak on-axis E_{dep} from the main pulse). Expectedly, as the provided plasma density decreases below a certain threshold ($n_p \sim 10^{10}$ cm^{-3} and $T_p = 0$ eV, here), the minimum r_b^{foc} and peak on-axis E_{dep} for the main 3 ns pulse decrease as well, although the $I_b^{\mathrm{max}}/I_0 = 67$ is recovered in each case within a few cm of the intended focal plane (recall the same in the cases lacking plasma). The cumulative partial neutralization effects caused by the partially exposed beam potential within the drift length contribute to beam emittance growth (up to a factor of approximately 3, here) and ultimately deteriorate the quality of the focal plane.

The $n_p = 10^{10}$ cm^{-3} plasma density case traps electrons in the beam potential and recovers the completely neutralized result even though the peak on-axis beam density is over an order of magnitude larger ($n_b^{\mathrm{foc}} \sim 2.3 \times 10^{11}$ cm^{-3}) than the provided plasma density. The reason for this result is found in the artificially cold initial $T_p =$ 0 eV.

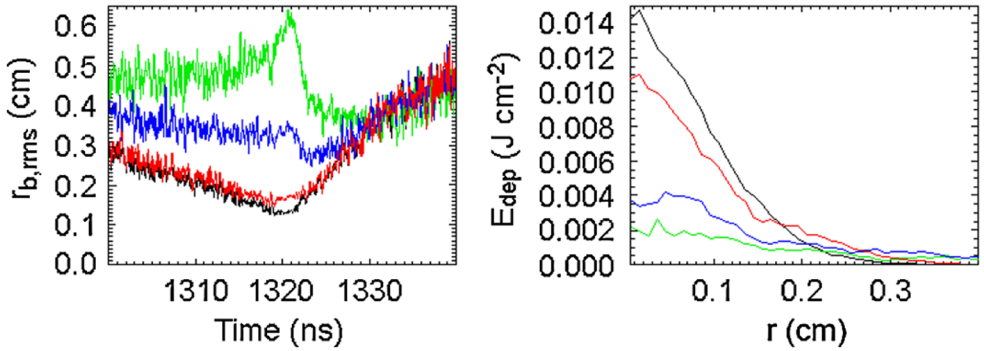

FIG. 27. (Color) Time history plots of rms $r_b(t)$ (left) and radial profiles of cumulative $E_{\mathrm{dep}}(r)$ for the main pulse from $t =$ 1319–1322 ns (right) at the focal plane using an initial $\Delta\theta_r = -32.3$ mrad and $n_p = 10^{10}$ cm^{-3} (black), 10^9 cm^{-3} (red), 10^8 cm^{-3} (blue), and 10^7 cm^{-3} (green) with initial $T_p = 0$ eV. The $n_p = 10^{11}$ and 10^{12} cm^{-3} cases (not shown) are identical to the $n_p =$ 10^{10} cm^{-3} case (and completely neutralized case).

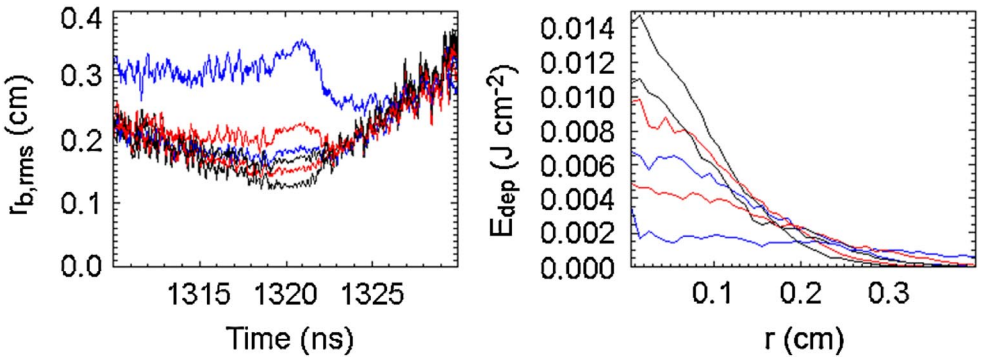

FIG. 28. (Color) Time history plots of rms $r_b(t)$ (left) and radial profiles of cumulative $E_{\mathrm{dep}}(r)$ for the main pulse from $t =$ 1319–1322 ns (right) at the focal plane using an initial $\Delta\theta_r = -32.3$ mrad and $n_p = 10^{10}$ cm^{-3} (bottom profiles on left, top profiles on right) and $n_p = 10^9$ cm^{-3} (top profiles on left, bottom profiles on right) with initial $T_p = 0$ eV (black), $T_p = 10$ eV (red), and $T_p = 50$ eV (blue).

Next, a sequence of PIC simulations is calculated to quantify the partial neutralization effects from variations in initial plasma temperature. The overfocused simulation from Sec. VA is repeated in the presence of initialized spatially uniform plasmas with $n_p = 10^{10}$ cm^{-3} and 10^9 cm^{-3}, and with initial plasma temperatures $T_p =$ 10 eV and 50 eV, located from $z = +5$ cm to $z =$ $+110$ cm. A warm electron emission model in LSP emits those particles with $T_e = T_p$ from the conducting wall at $r_w = 3.8$ cm and provides a copious supply of electrons at the sheath, as in the cold emission model described previously.

The simultaneous compression results from the cases of various initialized plasma temperatures T_p for the plasma density cases $n_p = 10^{10}$ and 10^9 cm^{-3} are plotted in Fig. 28. The case with $n_p = 10^{10}$ cm^{-3} and initial $T_p =$ 0 eV recovers the completely neutralized results. As the initial T_p increases, the minimum r_b^{foc} increases and the peak on-axis E_{dep} for the main pulse decreases, although $I_b^{\max}/I_0 = 67$ is recovered in each case within a few cm of the intended focal plane (recall the same in the cases lacking plasma). The cumulative partial neutralization effects caused by the partially exposed beam potential in the plasmas with finite temperature contribute to the quality degradation of the focal plane.

TABLE I. Simultaneous compression dependence on T_p.

n_p	T_p	Minimum r_b^{foc} (rms)	λ_D	$r_b^{\mathrm{foc}} - \lambda_D$
10^{10} cm^{-3}	0 eV	0.125 cm	0 cm	0.125 cm
10^{10} cm^{-3}	10 eV	0.151 cm	0.024 cm	0.127 cm
10^{10} cm^{-3}	50 eV	0.181 cm	0.053 cm	0.128 cm
10^9 cm^{-3}	0 eV	0.166 cm	0 cm	0.166 cm
10^9 cm^{-3}	10 eV	0.220 cm	0.074 cm	0.146 cm
10^9 cm^{-3}	50 eV	0.334 cm	0.166 cm	0.168 cm

Table I presents the rms r_b^{foc} for the cases in Fig. 28 involving variations in initial plasma density and temperature. The difference between the r_b^{foc} and Debye length λ_D is evaluated, and the fifth column demonstrates that partial neutralization effects due to T_p increase the r_b^{foc} from the respective cold plasma cases by approximately adding to them the corresponding λ_D, for the parameters considered here. In practice, $T_p(r, z, t)$ may take on a wide range, suggesting the use of $n_p \gg n_b$ in experiments to ensure $r_b^{\mathrm{foc}} \gg \lambda_D$ and high levels of neutralization.

The ferroelectric source provides less neutralization than expected, since the maximum plasma density and minimum plasma temperature are 2.5×10^{10} cm^{-3} and 20 eV, respectively, but the cumulative energy deposition from the main pulse in that case ($E_{\mathrm{dep}} \sim 0.003$ J cm^{-2}, refer to Fig. 26) is only as good as the $n_p = 10^9$ cm^{-3} plasma density case of Fig. 28 with a plasma temperature in the range 10–50 eV. Assessment of the cause for the excess loss of neutralization in the case of the dynamic FEPS requires further research. The three primary differences between the constant plasma density cases and the ferroelectric plasma are the (1) time-dependent nature of the dynamic ferroelectric $n_p(t)$, (2) four regions of decreased ferroelectric plasma density due to the transverse ports (refer to Fig. 25 and Sec. III), and (3) significant directed radial momenta of the ferroelectric plasma ions, which are of the same order as the radial momenta of the beam ions.

VI. SUMMARY AND CONCLUSIONS

In support of experimental efforts on the neutralized drift compression experiment (NDCX), large-space-scale and long-time-scale numerical PIC simulations have been executed in order to study the spatial and temporal evolution of the plasma flow from two different types of sources used in the laboratory, since they were responsible for the achieved degree of beam neutralization within the drift

length. Furthermore, the simulations of plasma injection into the NDCX device have allowed evaluation of realistic parameters achieved in the experiments, so they can be employed in more sophisticated compression simulations, which previously assumed constant plasma density and temperature profiles and neglected the dynamical nature of the background plasma. The simulations provide increased confidence that sufficient levels of plasma density were present in the longitudinal beam compression experiments.

In the NDCX device, a filtered cathodic-arc plasma source (FCAPS) creates and injects highly ionized, supersonic plasma jets into the system along externally imposed magnetic field lines (Sec. II). The simulated plasma was injected into the 3D magnetic topology composed of two solenoidal filter coils ($B_z = 2$ kG) and a long guide solenoid ($B_z = 2$ kG) in the drift length (for confinement purposes). The PIC simulations provided self-consistent plasma flow evaluation in an otherwise challenging scenario. Perpendicular and parallel ∇B gradient drifts and curvature drifts were shown to affect the plasma dynamics. Using parameters relevant for present experiments on NDCX, an approximate 8% plasma density coupling efficiency from the sources to the drift region was calculated during steady-state flow, and the efficiency was argued to depend on many configuration parameters. In addition, 50% of the plasma arriving at the plane of the guide solenoid was found within it.

Numerical simulations of plasma flow from the $BaTiO_3$ ferroelectric plasma source (FEPS) evaluated the spatial and temporal dependence of the plasma density within the chamber under a variety of conditions (Sec. III). The main advantages of the ferroelectric source are the lack of required magnetic field for plasma confinement, which can alter the beam ion trajectories and affect neutralization processes, and the lack of upstream-directed plasma, which may penetrate into the acceleration gap and transport sections and increase the beam emittance. Three-dimensional simulations of the ferroelectric source, using measured load voltage and current profiles as initialization conditions, indicated that the radially injected plasma uniformly filled the drift length in approximately $t \sim 6$ μs, including plasma flow into the transverse diagnostic access gaps (with reduced density). Agreement with experimental measurements was achieved using an effective mass $m_i^{\text{eff}} = 3 \times \text{Ba}$ for the plasma ions and initialized $T_e = T_i = 20$ eV. The comparison was qualitative since the problem did not necessarily have a unique solution, due to a number of free parameters, including the ion mass and temperature. Simulations involving azimuthally asymmetric plasma production at the source walls showed that symmetric profiles were nevertheless achieved at the times of peak on-axis plasma density. Finally, contrary to the axially injected cathodic-arc plasma, the radially injected ferroelectric plasma only expanded upstream due to thermal expansion, and avoided the possibility of allowing electrons to move upstream beyond the intended plasma column and partially neutralize the beam during its neutral transport.

Strong final-focus solenoids will be used in upcoming experiments on NDCX in order to transversely focus the axially compressing beam to a coincident focal plane with a sub-mm spot size. In order to fill a final-focus solenoid with the requisite amount of high-density plasma for beam neutralization, simulations were executed in order to predict the amount of plasma fill due to injection of the plasma from the low-field region (Sec. IV). Evidence was shown for significant magnetic mirroring of the injected plasma in the transition region leading up to the $B_z = 53$ kG and $B_z = 40$ kG final-focus solenoids in 3D and 2D models, respectively. Plasma partially filled the solenoids near the $r = 0$ axis to radii $r_p^{\text{fill}} \leq 0.6$ cm. Significant plasma density compression was evident in the vicinity of the focal plane, which was expected to provide additional neutralization otherwise not achievable from the cathodic-arc source. Larger ion injection velocities corresponded to higher penetrating plasma densities into the final-focus solenoid, and significant counterpropagating streams of ions were observed on the downstream end of the solenoids due to magnetic mirroring. Also, maximum plasma density and minimum average plasma flow velocity were witnessed at the downstream end of the final-focus solenoids.

Experiments are planned to measure whether the injected plasma can fill such strong solenoids, and provide quantitative comparisons to the predictions in the simulations. Since the beam radius $r_b(t)$ may be larger than the on-axis plasma fill factor as it enters the solenoid, whether a partially filled final-focus solenoid is sufficient for high levels of beam neutralization during simultaneous focusing is an important issue which requires additional research. In addition, further investigation is needed to determine whether the plasma that enters the final-focus solenoid can effectively neutralize the beam, which depends largely on design considerations such as beam density $n_b(t)$, beam radius $r_b(t)$, and whether the focal plane resides within (or downstream of) the final-focus solenoid. Full-fill scenarios involving multiple plasma sources injecting plasma along a variety of field lines are also suggested for future research.

Since the application of a longitudinal velocity tilt in the acceleration gap was responsible for time-dependently defocusing the radial trajectories of the beam ions due to an imbalance in the integrated electric field, the beam was given an ''overfocused'' initial convergence angle $\Delta\theta_r$ in order to offset the defocusing effect in an average way (Sec. V A). The technique also ensured that the majority of the cumulative energy deposition resided within the main compressed pulse. In the absence of neutralizing plasma, the intense self-fields of the beam caused radial expansion to an unusable spot size for warm dense matter and heavy ion fusion applications (Sec. V B). Simultaneous compres-

sion results were presented for parametric changes involving the assumed background plasma density and temperature, as well as a beam compression case including the realistic dynamical evolution of the plasma generated by the ferroelectric plasma source. Global changes in plasma density and temperature demonstrated that reduced plasma densities and increased temperatures were detrimental to the compression results, since the neutralization physics occurs on a Debye-length scale λ_D. The cumulative effects of partial neutralization on charge bunch compression, caused by partially exposed beam potential within the drift length, increased the minimum radius and decreased the energy deposition capability of the beam at the simultaneous focal plane. To a lesser extent, the beam's pulse length at focus, the emittance growth due to partial neutralization, and the separation of focal plane locations were also witnessed. In practice, plasma temperatures may take on a wide range of values in space and time, suggesting the use of plasma densities much greater than the beam density throughout the drift length in experiments (as in previous publications), in order to ensure $r_b^{\mathrm{foc}} \gg \lambda_D$ and provide high levels of charge neutralization for focusing of the charge bunch.

ACKNOWLEDGMENTS

This research was supported by the U.S. Department of Energy under the auspices of the Heavy Ion Fusion Science Virtual National Laboratory. The authors would like to acknowledge useful discussions with Dr. P. C. Efthimion, Dr. A. Friedman, Dr. J.-Y. Jung, Dr. I. D. Kaganovich, Dr. M. Leitner, Dr. P. K. Roy, Dr. P. A. Seidl, Dr. E. A. Startsev, Dr. D. R. Welch, and Dr. . S. Yu with special thanks to A. Carpe for technical assistance.

[1] P. K. Roy, S. S. Yu, E. Henestroza, A. Anders, F. M. Bieniosek, J. Coleman, S. Eylon, W. G. Greenway, M. Leitner, B. G. Logan, W. L. Waldron, D. R. Welch, C. Thoma, A. B. Sefkow, E. P. Gilson, P. C. Efthimion, and R. C. Davidson, Phys. Rev. Lett. **95**, 234801 (2005).

[2] I. D. Kaganovich, G. Shvets, E. Startsev, and R. C. Davidson, Phys. Plasmas **8**, 4180 (2001).

[3] D. R. Welch, D. V. Rose, B. V. Oliver, and R. E. Clark, Nucl. Instrum. Methods Phys. Res., Sect. A **464**, 134 (2001).

[4] D. R. Welch, D. V. Rose, W. M. Sharp, and C. L. Olson, Laser Part. Beams **20**, 621 (2002).

[5] C. H. Thoma, D. R. Welch, S. Eylon, E. Henestroza, P. K. Roy, S. S. Yu, and E. P. Gilson, Proceedings of the 2005 Particle Accelerator Conference (IEEE, New York, 2005), p. 3765, http://ieeexplore.ieee.org/xpls/abs_all.jsp?arnumber=1591698.

[6] D. R. Welch, D. V. Rose, T. C. Genoni, S. S. Yu, and J. J. Barnard, Nucl. Instrum. Methods Phys. Res., Sect. A **544**, 236 (2005).

[7] A. B. Sefkow and R. C. Davidson, Phys. Rev. ST Accel. Beams **9**, 090101 (2006).

[8] A. B. Sefkow, R. C. Davidson, I. D. Kaganovich, E. P. Gilson, P. K. Roy, P. A. Seidl, S. S. Yu, D. R. Welch, D. V. Rose, and J. J. Barnard, Nucl. Instrum. Methods Phys. Res., Sect. A **577**, 289 (2007).

[9] D. R. Welch, D. V. Rose, C. H. Thoma, A. B. Sefkow, I. D. Kaganovich, P. A. Seidl, S. S. Yu, and P. K. Roy, Nucl. Instrum. Methods Phys. Res., Sect. A **577**, 231 (2007).

[10] A. B. Sefkow and R. C. Davidson, Phys. Rev. ST Accel. Beams **10**, 100101 (2007).

[11] C. K. Birdsall and A. B. Langdon, *Plasma Physics via Computer Simulation* (McGraw-Hill Book Company, New York, 1985).

[12] T. P. Hughes, S. S. Yu, and R. E. Clark, Phys. Rev. ST Accel. Beams **2**, 110401 (1999).

[13] D. R. Welch, D. V. Rose, R. E. Clark, T. C. Genoni, and T. P. Hughes, Comput. Phys. Commun. **164**, 183 (2004).

[14] LSP is a software product of ATK Mission Research, Albuquerque, NM 87110.

[15] A. B. Sefkow, Ph.D. thesis, Princeton University, 2007. http://www.pppl.gov/~asefkow/thesis/.

[16] E. Henestroza, S. Eylon, P. K. Roy, S. S. Yu, A. Anders, F. M. Bieniosek, W. G. Greenway, B. G. Logan, R. A. MacGill, D. B. Shuman, D. L. Vanecek, W. L. Waldron, W. M. Sharp, T. L. Houck, R. C. Davidson, P. C. Efthimion, E. P. Gilson, A. B. Sefkow, D. R. Welch, D. V. Rose, and C. L. Olson, Phys. Rev. ST Accel. Beams **7**, 083501 (2004).

[17] R. A. MacGill, M. R. Dickinson, A. Anders, O. R. Monteiro, and I. G. Brown, Rev. Sci. Instrum. **69**, 801 (1998).

[18] A. Anders, Surf. Coat. Technol. **120–121**, 319 (1999).

[19] A. Anders and G. Y. Yushkov, J. Appl. Phys. **91**, 4824 (2002).

[20] Acree Technologies Incorporated (private communication).

[21] B. Juttner, IEEE Trans. Plasma Sci. **PS-15**, 474 (1987).

[22] C. Wieckert, Contrib. Plasma Phys. **25**, 309 (1987).

[23] M. K. Covo, A. W. Molvik, A. Friedman, G. Westenskow, J. J. Barnard, R. Cohen, P. A. Seidl, J. W. Kwan, B. G. Logan, D. Baca, F. Bieniosek, C. M. Celata, J.-L. Vay, and J. L. Vujic, Phys. Rev. ST Accel. Beams **9**, 063201 (2006).

[24] M. K. Covo, A. W. Molvik, A. Friedman, J.-L. Vay, P. A. Seidl, B. G. Logan, D. Baca, and J. L. Vujic, Phys. Rev. Lett. **97**, 054801 (2006).

[25] R. J. Goldston and P. H. Rutherford, *Introduction to Plasma Physics* (Institute of Physics Publishing, Bristol and Philadelphia, 1995).

[26] J. Y. Jung (private communication).

[27] VECTOR FIELDS OPERA-3D is a software product of Vector Fields Inc., Aurora, IL 60505, http://www.vectorfields.com.

[28] F. F. Chen, *Plasma Physics and Controlled Fusion* (Plenum Press, New York, 1984).

[29] G. Y. Yushkov, A. Anders, E. M. Brown, and I. G. Brown, J. Appl. Phys. **88**, 5618 (2000).

[30] G. Rosenman, D. Shur, Y. E. Krasik, and A. Dunaevsky, J. Appl. Phys. **88**, 6109 (2000).

[31] A. Dunaevsky, Y. E. Krasik, J. Felsteiner, and A. Sternlieb,

J. Appl. Phys. **90**, 3689 (2001).
[32] A. Dunaevsky and N. J. Fisch, J. Appl. Phys. **95**, 4621 (2004).
[33] P. C. Efthimion, E. P. Gilson, L. Grisham, R. C. Davidson, S. S. Yu, W. L. Waldron, and B. G. Logan, Nucl. Instrum. Methods Phys. Res., Sect. A **544**, 378 (2005).
[34] P. C. Efthimion, E. P. Gilson, L. Grisham, R. C. Davidson, S. S. Yu, W. L. Waldron, and B. G. Logan, Proceedings of the 2005 Particle Accelerator Conference (IEEE, New York, 2005), p. 2452, http://ieeexplore.ieee.org/xpls/abs_all.jsp?arnumber=1591142.
[35] P. C. Efthimion, E. P. Gilson, R. C. Davidson, L. Grisham, B. G. Logan, P. A. Seidl, W. L. Waldron, and S. S. Yu, Nucl. Instrum. Methods Phys. Res., Sect. A **577**, 203 (2007).
[36] A. Dunaevsky, Y. E. Krasik, J. Felsteiner, S. Dorfman, A. Berner, and A. Sternlieb, J. Appl. Phys. **89**, 4480 (2001).
[37] A. B. Sefkow, R. C. Davidson, P. C. Efthimion, E. P. Gilson, S. S. Yu, P. K. Roy, F. M. Bieniosek, J. E. Coleman, S. Eylon, W. G. Greenway, E. Henestroza, J. W. Kwan, D. L. Vanecek, W. L. Waldron, and D. R. Welch, Phys. Rev. ST Accel. Beams **9**, 052801 (2006).
[38] B. I. Cohen, A. B. Langdon, and A. Friedman, J. Comput. Phys. **46**, 15 (1982).
[39] D. W. Hewett and A. B. Langdon, J. Comput. Phys. **72**, 121 (1987).
[40] A. Friedman, J. Comput. Phys. **90**, 292 (1990).
[41] C. H. Thoma, Mission Research Corporation MRC/ABQ-R-2070, 1, 2002.
[42] P. A. Seidl, J. Armijo, D. Baca, F. M. Bieniosek, J. E. Coleman, E. Henestroza, M. Leitner, B. G. Logan, P. K. Roy, W. L. Waldron, S. S. Yu, A. Friedman, M. Kireeff-Covo, D. Grote, A. W. Molvik, W. M. Sharp, J. L. Vay, I. Haber, A. B. Sefkow, E. P. Gilson, P. C. Efthimion, I. D. Kaganovich, R. C. Davidson, D. V. Rose, and D. R. Welch, Nucl. Instrum. Methods Phys. Res., Sect. A **577**, 215 (2007).